A spatially orthogonal hierarchically porous acid-base catalyst for cascade and antagonistic reactions

Mark A. Isaacs,[1,2] Christopher M.A. Parlett,[3,4,5] Neil Robinson,[6] Lee J. Durndell,[7] Jinesh Manayil,[8] Simon K. Beaumont,[9] Shan Jiang,[9] Nicole S. Hondow,[10] Alexander C. Lamb,[11] Deshetti Jampaiah,[11] Michael L. Johns,[6] Karen Wilson[11]* and Adam F. Lee[11]*

[1]Department of Chemistry, University College London, London WC1H 0AJ, UK
[2]HarwellXPS, Research Complex at Harwell, Rutherford Appleton Laboratories, Didcot OX11 0FA, UK
[3]Department of Chemical Engineering and Analytical Science, University of Manchester, Manchester M13 9PL, UK
[4]University of Manchester at Harwell, Diamond Light Source, Harwell Science and Innovation Campus, Didcot OX11 0DE, UK.
[5]Diamond Light Source, Harwell Science and Innovation Campus, Didcot OX11 0DE, UK.
[6]Department of Chemical Engineering, University of Western Australia, Perth WA6009, Australia
[7]School of Geography, Earth and Environmental Sciences, University of Plymouth, Plymouth PL4 8AA, UK
[8]European Bioenergy Research Institute, Aston University, Birmingham B4 7ET, UK
[9]Department of Chemistry, Durham University, Durham DH1 3LE, UK
[10]School of Chemical and Process Engineering, University of Leeds, Leeds LS2 9JT, UK
[11]School of Science, RMIT University, Melbourne VIC3000, Australia

Abstract

Complex organic molecules are of great importance to academic and industrial chemistry and typically synthesised from smaller building blocks by multistep reactions. The ability to perform multiple (distinct) transformations in a single reactor would greatly reduce the number of manipulations required for chemical manufacturing, and hence the development of multifunctional catalysts for such one-pot reactions is highly desirable. Here we report the synthesis of a hierarchically porous framework, in which the macropores are selectively functionalised with a sulfated zirconia solid acid

coating, while the mesopores are selectively functionalised with MgO solid base nanoparticles. Active site compartmentalisation and substrate channelling protects base catalysed triacylglyceride transesterification from poisoning by free fatty acid impurities (even at 50 mol%), and promotes the efficient two-step cascade deacetylation-Knoevenagel condensation of dimethyl acetals to cyanoates.

Catalysis is a cornerstone of green chemistry, enabling energy and resource efficient synthesis of fine and specialty chemicals through selective transformations which minimise by-product and waste formation, eliminate the necessity for auxiliaries, and facilitate product separation. Multistep synthesis of complex molecules is fraught with limitations arising from the costly and time-consuming isolation and purification of intermediates, and hence ripe for substantial improvements in energy and atom efficiency. The ability to perform one-pot cascade processes involving one or more catalysts for multistep synthesis is particularly attractive, offering fewer unit operations, reduced solvent and energy inputs and associated product losses,[1,2] and unlocking new processes utilising impure feedstocks[3] or intermediates that are difficult to isolate.[4-6] Integrated product formation during the simultaneous conversion of mixed feedstocks over different catalysts is another area where scientific and technological advances are required to reduce constraints on feedstock purity and by-product isolation.[7]

Multistep sequential reactions are ubiquitous in cell biology, wherein the transport of chemical intermediates between enzymes directs product formation via substrate channelling over inter-enzyme distances up to 10 nm.[8] Such coordination between active sites requires efficient molecular diffusion, and attempts to replicate substrate channelling in homogeneous or heterogeneous catalysis has proved challenging, requiring precise control over the spatial distribution and connectivity of the catalytic species to optimise diffusion paths. In this context, tandem catalysis is defined as a process in which sequential reactant transformations occurs by at least two distinct mechanisms, with all catalytic species present at the beginning of the reaction.[9] For homogeneous transformations, single catalysts

operating by auto-tandem or assisted tandem approaches are prone to by-product formation or require a perturbation in reaction conditions to trigger subsequent steps.[9] Auto-tandem catalysis is considered the more attractive approach since the temporal separation of catalytic steps[10] (wherein conversion of an intermediate awaits full conversion of the substrate) may reduce by-product formation. In contrast, orthogonal tandem catalysis involves multiple, non-interfering catalytic sites that can diversify accessible transformations,[11] however negative interactions between incompatible catalytic species (or substrates/reactively-formed intermediates and active sites) has hindered this approach (**Figure 1**). Methodology to segregate/compartmentalise active sites for so-called spatially orthogonal catalysis is hence of significant interest in organic synthesis, and a hot topic in porous materials design.

Cooperative effects in bifunctional catalysts may be classified into systems wherein: multiple active sites are randomly distributed throughout the catalyst;[12-15] multiple active sites located in different parts of a catalyst but operate independently;[16,17] or multiple active sites in immediate proximity participating in same reaction.[18-20] However, despite their elegance, none of these synthetic strategies can control the sequence in which reactants interact with individual active sites. Such control is critical for antagonistic reactions wherein one component of a reaction mixture may interfere with the reaction of other components, and a key feature of biological catalysis (substrate channelling).

Bifunctional acid-base catalysts have been widely studied in recent years,[21] with spatial segregation exploited to incorporate these chemically incompatible sites in a single material.[16,22-24] Core-shell nanostructures have proven popular in efforts to control the reaction sequence,[25,26] but rely on incorporating one catalytic function over the external surface of e.g. porous silica spheres,[27] resulting in low active site densities. More sophisticated analogues have employed acid-functionalised mesoporous cores encapsulated by base-functionalised mesoporous shells,[24] or yolk-shell systems with basic amine cores and silica sulfonic acidic shells to increase active site loadings in the shell.[28] However, all such spatially orthogonal catalysts utilise organic acids-bases of limited thermal stability (typically <200 °C),[29] and their intrinsic microporosity or mesoporosity[17,30] is problematic for the

transformation of bulky biomass-derived substrates. Efforts to coat (basic) Mg-Al layered double hydroxide cores with porous (acidic) Al-MCM shells[25] are compromised by entrained alkali from NaOH during synthesis, and limited accessibility of base sites between microporous layers.

Solid acids and bases catalyse diverse organic transformations:[31-35] esterification, isomerisation, dehydration, Friedel-Crafts acylation/alkylation, ring-opening, and hydrocarbon cracking for the former; transesterification, aldol-condensation, Michael and Henry addition, double-bond migration, and dehydrogenation for the latter. Solid bases are particularly efficient for the transesterification of triacylglycerides (TAGs) with methanol under mild conditions to produce fatty acid methyl esters (FAMEs), the key component of biodiesel.[36] However, free fatty acids (FFAs), which typically constitute 1-20 wt% of non-edible or waste oleaginous feedstocks,[37] rapidly poison base active sites. One solution is to introduce an acid catalysed esterification pretreatment to transform these problematic FFAs into additional FAME, prior to transesterification of the TAG component.[38] Nonetheless, this approach necessitates rigorous separation of the acid catalyst and/or neutralisation of the resulting TAG/FAME product stream to avoid subsequent base catalyst deactivation, lowering overall process atom and energy efficiency.[3] Tandem acid-base catalytic cascades are important for fine chemical and natural product synthesis,[39] with transformations spanning hydrolysis-condensation for the synthesis of benzylidene malononitrile from benzaldehyde dimethylacetal,[17] to Michael addition-aldol condensation for the synthesis of alkaloid intermediates in Alzheimer's treatments.[40] In biomass valorisation, cascades include the synthesis of fructose from cellulose by hydrolysis-isomerisation,[41] 5-HMF or alkyl-levulinate synthesis from glucose by respective isomerisation-dehydration or condensation-isomerisation. Cooperative aldol condensation via base catalysed condensation and subsequent acid catalysed dehydration is also known.[14] Early attempts at such one-pot cascades used physical mixtures of solid acid and base catalysts,[30,42] or co-derivatised materials in which active sites were randomly distributed[43] and/or partially sacrificed during the catalyst synthesis.[44] Subsequent efforts to partition acid and base functions have employed isolated polymer

capsules for enolization-acylation,[45] or non-penetrating dendritic star polymers to encapsulate or isolate separate active sites for iminium, enamine, and hydrogen-bond formation in asymmetric synthesis.[46]

We recently reported the fabrication of a spatially orthogonal hierarchically porous catalyst, conceptually illustrated in **Figure 1**,[47] for which the cascade selective aerobic oxidation of cinnamyl alcohol to cinnamic acid overcomes the limitations outlined above. Selective detemplation and post-functionalisation of a macroporous SBA-15 silica framework permitted the exclusive confinement of Pd nanoparticles (active for allylic alcohol oxidation to aldehydes) within macropores and Pt nanoparticles (active for allylic aldehyde oxidation to acids) within the mesopores. However, this route required macropore hydrophobisation to differentiate the surface chemistry of the two pore networks, increasing the complexity of the synthesis and hindering transformations in polar environments.

Here we adopt a different methodology, using a metallosurfactant to template (and thereby directly introduce a catalytic function into) the mesopores from the outset, obviating the need for additional surface derivatisation and ensuring spatial compartmentalisation of chemically distinct active sites. This approach is demonstrated for the synthesis of a spatially orthogonal (inorganic) acid-base catalyst, SZ/MgO/MM-SBA-15, comprising nanoparticulate MgO within mesopores and a conformal sulfated zirconia (SZ) monolayer coating macropores, and its application for the one-pot transesterification of fatty acid contaminated bio-oils and cascade reactions.

Results

Synthesis of spatially orthogonal acid-base pore framework. A hierarchical macroporous-mesoporous SBA-15, containing spatially segregated acid (sulfated zirconia) and base (MgO nanoparticles) catalytic sites, was synthesised by adapting our previously reported dual templating strategy[47] (**Figure 2**) to incorporate one chemical function directly into the lyotropic liquid crystal template (rather than by post-functionalisation). The ability of Pluronic P123 to coordinate Mg^{2+}

cations through the polyethylene oxide head groups[48] was exploited through the addition of magnesium nitrate to a lyotropic liquid crystal ordered mesophase (**Figure 2a**), which acted as a soft template for subsequent infiltration by a silica network grown through the acid hydrolysis of tetramethoxyorthosilane. Monodispersed 400 nm polystyrene nanospheres in a crystalline matrix were introduced during the early stage of silica network condensation as a macropore-directing hard template. Sub-ambient extraction of the polystyrene nanospheres from the resulting hybrid organic-inorganic framework with toluene to create a macropore array (**Figure 2b**) was confirmed by thermogravimetric analysis and porosimetry. These mild extraction conditions achieved 95 % removal of the polystyrene macropore template, while retaining 98 % of the P123 mesopore template (see **Supplementary Figure 1**); no mesopores were detectable by N_2 physisorption (see **Supplementary Figure 2a**). The macropore network was then selectively functionalised by zirconium isopropoxide, which in turn was hydrolysed to form a $Zr(OH)_4$ conformal monolayer[49] (**Figure 2c**) and sulfated to introduce Brønsted acidity (**Figure 2d**). Nitrogen porosimetry confirmed that the mild conditions employed in these latter steps preserved the P123 mesopore template throughout the silica framework (see **Supplementary Figure 2a**). A final calcination served to burn out the surfactant template (see **Supplementary Figure 3**), thereby creating an open mesopore network of 4 nm channels, evidenced by the emergence of a type-IV adsorption-desorption isotherm with H1 hysteresis and associated narrow mesopore size distribution (see **Supplementary Figure 2a-b**), and to transform Mg and Zr species entrained within the meso- and macropores respectively into their corresponding oxides. Hg porosimetry and SEM (see **Extended Data Figure 1**) confirmed the formation of a hexagonal close-packed array of 350 nm macropores within the final material, interconnected by 50 nm windows, which we denote SZ/MgO/MM-SBA-15. Note that framework contraction following thermal processing shrinks macropore dimensions relative to their polystyrene hard template, as previously reported.[50]

Low angle powder X-ray diffraction (XRD) confirmed the formation of a *p6mm* hexagonal arrangement of ordered mesoporous channels (see **Supplementary Figure 4**), as previously reported

for macroporous SBA-15, however wide angle XRD provided no evidence of magnesium or zirconium containing crystalline phases, indicating that both elements were present in highly dispersed forms. Surface chemical analysis by X-ray photoelectron spectroscopy (XPS) was consistent with the formation of sulfated zirconia, and fitting of the O chemical environment revealed components characteristic of the silica framework and a stoichiometric sulfated zirconia adlayer (see **Supplementary Figure 5**). Quantitative comparison of Mg 2p XP spectra obtained using monochromated Al K_α (1486.69 eV) versus Ag L_α (2984.3 eV) excitation sources (see **Supplementary Figure 6**), confirmed that Mg lies deep within the SZ/MgO/MM-SBA-15 framework as anticipated for mesopore localisation. SZ/MgO/MM-SBA-15 was amphoteric (see **Extended Data Figure 2**), with an acid site density of 0.13 $mmol.g^{-1}$ and mixed Brønsted:Lewis character (0.75:1) from propylamine and pyridine titration respectively (see the **Methods** for further details), and a base site density of 45 $\mu mol.g^{-1}$ from CO_2 titration. These values, and corresponding acid and base strengths obtained from temperature programmed desorption, are in accordance with literature for sulfated zirconia monolayers[49] and MgO nanoparticles[51] subject to similar calcination treatments, and provide good evidence for the introduction of spatially orthogonal (non-interacting) acid-base functions. Note the relative acid:base site density does not mirror the relative macropore:mesopore surface areas. This likely reflects the different syntheses by which they are incorporated: Zr was introduced by a liquid phase atomic layer deposition route which conformally coats the available macropore surface area; in contrast, Mg is introduced through a metallosurfactant route in which the maximum metal content in the mesopores is restricted by the stability of the liquid crystal templating phase on cation chelation.

Note that the present strategy is fundamentally different from other approaches to create spatially orthogonal catalysts. Post-functionalisation methodologies require additional synthetic steps to chemically differentiate regions of pre-formed porous solids (whether interior versus exterior of mesopores,[16] or mesopore versus macropore networks[47]). Assembly of molecular precursors (e.g. hydrogelators) into interpenetrated networks necessitates the careful synthesis of components

possessing unique structural motifs that only self-sort, and not co-assemble,[12] and does not offer control over the sequence in which reactants/intermediates in a cascade encounter different active sites. These limitations restrict the range of catalytic functions that can be incorporated, and scope of chemical transformations accessible, by such approaches. In contrast, here we directly introduce chemical functionality into the organic mesophase (precursor to the inorganic mesopore network) at the start of the synthesis, through simple cation chelation. This strategy can be generalised to introduce diverse metal cations into the mesopores of hierarchical bimodal porous architectures, and eliminates complex and restrictive (synthetic) measures otherwise necessary to prevent interactions between chemical functions navigating to different destinations through pre-formed porous solids.

Visualisation of spatially orthogonal acid-base functions. The spatial distribution of Mg and Zr within SZ/MgO/MM-SBA-15 was mapped by scanning transmission electron microscopy (STEM) and energy dispersive X-ray spectroscopy (EDX). High-angle annular dark-field scanning transmission electron microscopy (HAADF-STEM) (**Figure 3a**) revealed enhanced contrast of macropore perimeters relative to mesoporous domains, which we attribute to stronger scattering from zirconia within the sulfated adlayer.[52] An EDX linescan across a mesopore domain bridged by two macropores (**Figure 3b)** also indicated the highest Zr and S concentrations occurred close to the macropore perimeters, whereas Mg was concentrated within the mesopores. Spatial compartmentalisation of Mg within the mesopores, and of Zr at the macropore perimeter, is more clearly evidenced by superposition and quantification of corresponding EDX elemental maps of a well-defined mesopore domain (**Figure 3c-e**). The atomic ratio of Zr:Mg averaged across the two regions indicated in **Figure 3d** is 12 times higher at the macropore boundaries than within the mesopore domain (**Figure 3f**), consistent with the selective coating of macropores by SZ. Note that areas where MgO appears to spillover at the vertices of the central mesopore domain in **Figure 3d** correspond to mesopore channels that encircle the macropores (apparent in **Figure 3c**).

Evidence that acid and base sites were respectively associated with SZ and MgO spatially segregated within macropores and mesopores, was obtained by the subsequent reactive grafting of ligand-stabilised Pt NPs as imaging contrast agents. Colloidal solutions of Pt NPs (see **Supplementary Figure 7**) synthesised with either 4-aminothiophenol or 3-mercaptopropionic acid ligands (coordinated to the metal surface through thiols) were reacted with SZ/MgO/MM-SBA-15 to selectively titrate acid or base sites respectively (see the **Methods** for further details). STEM imaging and EDX elemental mapping revealed that the amine base functionalised Pt NPs only accumulated at the perimeter of macropores, while carboxylic acid functionalised Pt NPs were confined within mesopores (see **Extended Data Figure 3a-f**).

Antagonistic acid-base catalysis. A spatially orthogonal hierarchical catalyst offers a unique approach to biodiesel production from FFA contaminated oleaginous feedstocks: namely a one-pot process in which acid catalysed esterification pretreatment of an FFA containing bio-oil feedstock occurs in the macropores, with the resulting (neutral) TAG/FAME mix diffusing into mesopores of the same particle to undergo base catalysed transesterification. This concept is demonstrated for the transesterification of tributyrin, a model TAG, in the presence of hexanoic acid, a model FFA, over SZ/MgO/MM-SBA-15, SZ/MM-SBA-15 (acid functionalised macropores) and MgO/MM-SBA-15 (base functionalised mesopores) analogues and a physical mixture thereof. Physicochemical characterisation of these monofunctional materials revealed similar textural and acid/base properties, compositions, and spatial localisation of functions within macropore/mesopore networks (see **Extended Data Figures 1 & 2, Supplementary Figure 8, and Supplementary Tables 1 & 2**).

Sulfated zirconia and MgO are independently active solid acid and base catalysts respectively for hexanoic acid esterification with methanol[35] and tributyrin transesterification with methanol (**Figure 4**),[36] however neither SZ/MM-SBA-15 nor MgO/MM-SBA-15 can efficiently effect the counterposing

reaction (see **Supplementary Figure 9**). In contrast, SZ/MgO/MM-SBA-15 is active for both reactions, exhibiting similar rates for hexanoic acid esterification and tributyrin transesterification to those obtained over SZ/MM-SBA-15 and MgO /MM-SBA-15 respectively. The co-existence of SZ and MgO catalytic functions within a single catalyst particle is achieved without detriment to the performance of either, strongly evidencing their segregation within macropores (acid) and mesopores (base).

The unique advantage of a spatially orthogonal acid-base catalyst become apparent when tributyrin transesterification is attempted in the presence of hexanoic acid (as observed in **Figure 5a** and **Supplementary Figure 10** and **Supplementary Table 3**). Transesterification is strongly poisoned by FFA addition over MgO/MM-SBA-15, a physical mixture of SZ/MM-SBA-15 with MgO/MM-SBA-15, and a non-porous MgO functionalised SZ (see **Extended Data Figure 4**), due to neutralisation of MgO base sites. The latter observations highlight that acid sites in a different particle, or co-located at the surface of the same particle (see **Supplementary Figure 11**), offer no protection for base sites. In contrast, SZ/MgO/MM-SBA-15 is resistant to 50 mol% (28 wt%) FFA addition (**Figure 5a**). This resistance to FFA poisoning reflects that: base sites are overwhelmingly located in the mesopores (**Figure 3** and **Extended Data Figure 3**); and mesopores are only accessible through the macropores, the latter being acid-functionalised and hence neutralising the FFA by esterification (see **Supplementary Figure 10e**) before it can enter the mesopore). Such a molecular transport process, the movement of reactants from the bulk solution into macropores and subsequently from macropores to mesopores, constitutes substrate channelling (**Figure 5b**).

Molecular transport investigation via NMR. A key element of substrate channelling is control over the sequence in which reactants/products access different active sites. NMR relaxation and diffusion experiments are powerful methods for the non-invasive investigation of adsorption and transport phenomena occurring within optically-opaque porous catalysis materials.[53-55] Low-field ^{1}H relaxation-

exchange correlation measurements were applied here to elucidate the dominant diffusive pathways present throughout our hierarchically porous MM-SBA-15 framework. The NMR pulse sequence for these experiments (see **Supplementary Figure 12**) is detailed in the **Supplementary Discussion**, and comprises two correlated measurements of the transverse nuclear spin relaxation time constant T_2 either side of a mixing time of length t_{mix}. As the T_2 of spin-bearing liquids confined to porous media is partially defined by the surface-to-volume (S/V) of the confining pore structure ($1/T_2 \propto S/V$, see **Supplementary Discussion**), this method is sensitive to the diffusive exchange of species between pores of different size, as well as between confined liquid within the pore structures and unrestricted bulk liquid outside of the material. Importantly, the use of low-field experiments facilitates the accurate measurement of T_2 by minimising undesired transverse relaxation effects resulting from magnetic susceptibility differences at the solid-liquid interface, which scale with magnetic field strength. An unfunctionalised framework was chosen to decouple molecular transport from surface chemistry, and water chosen as a probe molecule due to its high ^{1}H density, comparatively rapid self-diffusivity, and because its surface relaxation characteristics were optimal in differentiating the range of pore structures present (see **Supplementary Discussion**).

Relaxation-correlation data of our unfunctionalised framework in excess water was obtained at multiple mixing times between 50 ms and 2.5 s (**Figure 6**). Peak intensities indicate the relative probability of the system exhibiting a given combination of T_{2A} and T_{2B} time constants, which characterise the T_2 relaxation properties of the system before and after t_{mix}, respectively. Peaks along the $T_{2A} = T_{2B}$ diagonal therefore indicate water populations which remain within a given S/V during t_{mix}, while off-diagonal cross-peaks identify populations which undergo diffusive exchange during this time; the exchange pathways of these populations is found by identifying peaks with mutual relaxation coordinates. **Figure 6a** reveals four on-diagonal peaks, labelled A-D in order of decreasing T_2. The existence of four separate spin populations was further confirmed *via* a separate T_1-T_2 correlation measurement (see **Supplementary Figure 13**).[56] Given our knowledge of the MM-SBA-15 pore

network, and the sensitivity of T_2 to pore environments of different *S/V*, these peaks may be readily assigned to water located: (A) between MM-SBA-15 particles, (B) in macropores, (C) in mesopores, and (D) in micropores. Observation of a small micropore population is in accordance with reported microporosity in the pore walls of SBA-15,[57] and in agreement with pore size modelling in **Supplementary Figure 2c**. These peak assignments were further supported by separate measurements of water in mesoporous SBA-15 (data not shown) which exhibited peaks A, C and D only.

The low-intensity cross-peaks in **Figure 6a** were reproducible at short t_{mix} and are assigned to the diffusive exchange of water between micropores and both mesopores (peaks CD and DC) and macropores (BD and DB); the short t_{mix} time associated with the appearance of these cross-peaks confirms a short-range exchange process.[58] **Figure 6b-d** reveals additional cross-peaks (BC and CB) at slightly longer t_{mix}. Importantly, these cross-peaks identify exchange between mesopores and macropores, confirming the proposed pore connectivity (**Figure 5b**). **Figure 6c-d** report correlation data for long mixing times, which are required to observe long-range diffusive processes. **Figure 6c** suggests the onset of observable exchange between the macropore population and water outside of the MM-SBA-15 material is on the order of 1.5 s; this observation is supported by **Figure 6d** which shows clear AB and BA cross-peaks at t_{mix} = 2.5 s. Crucially, there is no evidence of exchange between mesopores and water outside of the material (AC or CA cross-peaks), which if occurring is expected to be observable within the range of t_{mix} values investigated; indeed the clear persistence of cross-peaks characterising mesopore↔macropore exchange (BC and CB) at long mixing times confirms that significant exchange processes involving the mesopore water population are readily observable using this approach. In summary, these results demonstrate that molecules in the bulk medium can only access active sites in the mesopores of our spatially orthogonal catalyst by first passing through macropores; a necessary condition for substrate channelling.

Cascade deacetalisation-Knoevenagel condensation. The catalytic advantage of our spatially orthogonal acid-base SZ/MgO/MM-SBA-15 material was also explored for the one-pot, two-step cascade transformation of benzaldehyde dimethyl acetal (BDMA) to benzylidene cyanoacetate (BCA) (**Figure 7a**). Benzaldehyde formed in the acid catalysed deacetalisation step may subsequently undergo a base catalysed Knoevenagel condensation with ethyl cyanoacetate to yield BCA. **Figure 7b-c** compares the performance of SZ/MgO/MM-SBA-15 with SZ/MM-SBA-15 (acid functionalised macropores) and MgO/MM-SBA-15 (base functionalised mesopores) analogues, and a physical mixture thereof.

Only catalyst configurations possessing acid sites were active for BDMA conversion (**Figure 7b**), while only those possessing base sites exhibited significant activity for benzaldehyde condensation with ethyl cyanoacetate (**Figure 7c**). The spatially orthogonal SZ/MgO/MM-SBA-15 showed comparable deacetalisation activity to SZ/MM-SBA-15 (see **Supplementary Table 4**), and comparable activity to MgO/MM-SBA-15 for the Knoevenagel condensation (see **Supplementary Table 5**). These similarities are also apparent in their 6 h conversions (**Figure 7**) demonstrating that our synthetic strategy successfully incorporated acid and base functions into the hierarchical porous framework without compromising the performance of either. In the Knoevenagel condensation alone (**Figure 7c**), both SZ/MgO/MM-SBA-15 and pure base MgO/MM-SBA-15 catalysts are 89 % to BCA, despite the presence of water (to mimic the cascade conditions). This compares favourably with amine functionalised silicas which achieve >95 % selectivity to BCA in organic solvents[59] or under solventless operation[60] to suppress hydrolysis of the cyanoester and avoid benzoic acid by-product formation.[60]

A physical mixture of the SZ/MM-SBA-15 and MgO/MM-SBA-15 monofunctional catalysts, possessing the same number of acid and base sites as SZ/MgO/MM-SBA-15, proved inefficient for the overall cascade, only achieving 26 % BCA yield from BDMA. This is close to the value (23 %) predicted if the probabilities of BDMA and reactively-formed benzaldehyde colliding with requisite

acid and base sites for their respective deacetalisation and condensation in the physical mixture were simply half those for reactions employing SZ/MM-SBA-15 and MgO/MM-SBA-15 alone (see **Supplementary Note 1**). Agreement between the observed and predicted BCA yields, wherein the latter neglects any potential acid-base synergy, indicates minimal interaction between discrete acid and base catalyst particles in the physical mixture. In contrast, SZ/MgO/MM-SBA-15 achieved 68 % BCA evidencing strong synergy between spatially orthogonal acid and base sites within the same catalyst particle. We attribute this synergy to the proximity of acid and base functions in SZ/MgO/MM-SBA-15, and hence increased probability that benzaldehyde reactively-formed from BDMA over SZ coated macropores will rapidly diffuse and encounter MgO nanoparticles within the mesopores, at which to couple with the cyanoester (i.e. substrate channelling). Similar performance enhancements for the spatially orthogonal acid-base SZ/MgO/MM-SBA-15 catalyst were also observed for anisaldehyde dimethyl acetal (ADMA) and 2-furaldehyde dimethyl acetal (FDMA) substrates (see **Extended Data Figure 5**), demonstrating a promising substrate scope.

The preceding examples highlight the versatility of spatially orthogonal catalysts for two mechanistically distinct applications. In the first, substrate channelling ensures that FFA molecules are neutralised (by esterification) in macropores, preventing them poisoning base sites within mesopores which therefore remain active for transesterification. In the second, cascade deacetalisation and Knoevenagel condensation is facilitated by locating base sites close to acid sites, thereby minimising diffusion paths for the reactively-formed benzaldehyde intermediate.

Conclusions

A strategy is reported for the fabrication of spatially orthogonal acid-base catalysts, in which pore hierarchy and metallosurfactant templating is exploited to segregate chemically incompatible catalytic sites. An acidic sulfated zirconia monolayer is grown within the macropores of a hierarchical SBA-15 silica framework, and basic magnesium oxide nanoparticles introduced into the connected mesopores.

Low-field NMR relaxation-exchange correlation measurements strongly evidence that the hierarchical nature and connectivity of the porous framework enables substrate channelling from a bulk reaction medium into macropores and subsequent molecular transport from macropores to mesopores. This architecture is uniquely suited to suppressing free fatty acid poisoning of triacylglyceride transesterification (pertinent to biodiesel production from low-grade feedstocks), and cooperative acid-base catalysis in the cascade synthesis of chemical intermediates. The combination of our route to spatially orthogonal porous materials and existing metallosurfactant templating literature provides opportunities to create diverse families of dual site catalysts for one-pot selective transformations.

Methods

Polystyrene colloidal nanospheres. Monodispersed non-crosslinked polystyrene spheres were produced following literature methods.[61] 105 cm^3 of styrene (99.9 %, Sigma Aldrich) was washed five times with 0.1 M sodium hydroxide solution (1:1 vol ratio of NaOH solution:styrene) and subsequently five times with distilled water (1:1 vol ratio) to remove polymerisation inhibitors. The purified styrene was added to 850 cm^3 of N_2 degassed de-ionised water at 80 °C, prior to the dropwise addition of 50 cm^3 of 0.24 M potassium persulfate (99+ %, Fisher) aqueous solution during 300 rpm agitation. After 22 h the solution turned white due to the formation of polystyrene colloidal nanospheres, which were recovered and processed into a crystalline matrix by centrifugation at 8,000 rpm/7,441 g for 1 h in a Hereus Multifuge X1centrifuge with a Thermo Fiberlite F15-8x50cy Fixed-Angle Rotor. The resulting highly ordered polystyrene crystalline matrix was finally ground to a fine powder in a mortar and pestle for use as a macropore-directing hard template.

Hierarchically ordered Mg functionalised SBA-15. A modified true liquid crystal templating approach[62] was used to prepare a Mg functionalised hierarchical SBA-15 silica framework. 2 g of Pluronic P123 (Sigma-Aldrich) was sonicated with 2 g of HCl acidified water (pH 2) at 40 °C to form a lyotropic H_1 liquid crystalline phase, to which 0.5 g of magnesium nitrate hexahydrate (98%, Sigma-Aldrich) was added. The resulting Mg^{2+} containing organic mesophase was then treated with 4.08 cm^3 tetramethoxysilane (99%, Sigma-Aldrich) and

stirred rapidly for 5 min at 800 rpm to form a homogeneous liquid. Immediately following this change in physical state the 400 nm polystyrene colloidal crystals (6 g ground to a fine powder) were added with agitation at 100 rpm for 1 min to homogenise the mix. The resulting viscous mixture was heated under 100 mbar vacuum at 40 °C for 2 h to remove methanol released during the hydrolysis. The solid was finally aged in air at room temperature for 24 h to complete condensation of the silica network.

Stepwise template extraction and macropore SZ functionalisation. Polystyrene template was extracted from the 10 g of the hard-soft templated silica by stirring in 100 cm^3 toluene (99 %, Sigma-Aldrich) at -8 °C for 1 min. The resulting solid was recovered by vacuum filtration and briefly washed with cold toluene. This extraction protocol was repeated four times to achieve complete removal of the polystyrene hard template. 1 g of the resulting macroporous silica (still containing P123) was then stirred in 30 cm^3 anhydrous hexane at 70 °C under flowing N_2 (1 $cm^3.min^{-1}$), prior to addition of 0.6 cm^3 zirconium isopropoxide (98 %, Fisher) This mixture was stirred 24 h, and 800 mg of the zirconium functionalised solid subsequently recovered by vacuum filtration. Zirconium isopropoxide functional groups were converted to hydroxyls via a hydrolysis step in which 800 mg of the previously isolated solid was dispersed with mild stirring in 25 cm^3 deionised water for 15 minutes before separation by filtration and drying overnight at 80 °C. Sulfation was achieved by the addition of 30 cm^3 of a 0.2 M solution of ammonium sulfate (99 %, Fisher) in isopropanol (98 %, Fisher), with the mixture stirred for 2 h, and the solid recovered by vacuum filtration and finally calcined at 400 °C (ramp rate of 1 $°C.min^{-1}$) for 10 h to remove the P123 mesopore template and form Mg and Zr oxides. The final material contained 2 wt% Zr, 1 wt% Mg, and 1.2 wt% S as determined by bulk elemental analysis (see **Supplementary Table 2**).

MgO/SZ control catalyst. A MgO/SZ control catalyst was prepared by wet impregnation of a non-porous SZ (MEL chemicals X201720/01, 99 %). The SZ was first calcined in air at 550 °C for 3 h (ramp rate of 5 $°C\ min^{-1}$). 2 g of $Mg(NO_3)_2.6H_2O$ (Aldrich, 98 %) was dissolved in 10 cm^3 of milli Q water and added to 0.5 g of calcined SZ in a 50 cm^3 3-neck round bottomed flask and stirred at 200 rpm for 2.5 h at room temperature. The flask was then heated at 80 °C overnight, and the resulting dry powder calcined in air at 550 °C for 3 h (ramp

rate of 5 °C min^{-1}) and the final sample stored in a vacuum desiccator. The Zr:Mg mass ratio determined by XRF was 1.60 ±0.01.

Platinum nanoparticle synthesis. Solvents were reagent grade and obtained from Fisher Scientific unless otherwise specified. Near monodisperse platinum nanoparticles of 3.6 ± 0.8 nm diameter were prepared using a procedure adapted from Mazumder and Sun.[63] Synthesis was carried out using standard Schlenk techniques under a nitrogen atmosphere. $Pt(acac)_2$ (50 mg, 0.13 mmol, Alfa Aesar) was added into a 3-neck round-bottom flask. The system was evacuated and refilled with N_2 (repeated three times). Oleylamine (OAm) (15 cm^3, Acros Organics, 80-90%) was added into the flask, and the mixed solution was heated to 100 °C while stirring for 20 min. Borane triethylamine complex (200 mg, 1.74 mmol, Aldrich, 97%) in 3 cm^3 OAm was then added into the Pt-OAm solution. The temperature was raised to 120 °C for 60 min. The reaction was cooled to room temperature, before addition of 30 cm^3 of ethanol, precipitating nanoparticles which could then be extracted by centrifugation (8000 rpm, 8 minutes, 50 cm^3 plastic centrifuge tube, prewashed with ethanol). The product was then dispersed in hexane. Ligand exchange was performed as follows. 4-Aminothiophenol (20 mg in 1 cm^3 chloroform solution, Sigma Aldrich) was added to approximately 5 mg of platinum nanoparticles prepared as above (by Pt wt.) dispersed in HPLC grade hexane (5 cm^3, Fisher) and stirred overnight at room temperature. The particles were isolated by centrifugation and washed with ethanol or acetone to remove excess 4-aminothiophenol and oleylamine. The same procedure was applied to 3-mercaptopropionic acid exchange but replacing the 4-aminothiophenol with 3-mercaptopropionic acid (Sigma Aldrich).

Reactive grafting of functionalised Pt nanoparticles. Functionalised Pt nanoparticles were incorporated into the SZ/MgO/MM-SBA-15 catalyst through a reactive grafting from hexane: 3.6 cm^3 of 0.017M functionalised Pt nanoparticles in hexane were added to 2.5 mg of the SZ/MgO/MM-SBA-15 catalyst and stirred for 10 min at 60 °C. The grafted catalyst was then filtered using a 0.2 μm syringe filter and washed three times with 3.6 cm^3 aliquots of hexane, dried and stored in a vacuum desiccator.

Materials characterisation. Nitrogen porosimetry was undertaken on a Quantachrome Autosorb IQTPX porosimeter with analysis using ASiQwin v3.01 software. Samples were degassed at 150 ºC for 12 h before recording N_2 adsorption/desorption isotherms. BET surface areas were calculated over the relative pressure range 0.02-0.2. Mesopore properties were calculated using either the BJH method applied to the desorption branch of the isotherm or fitting the desorption isotherm to the DFT (density functional theory) kernel within the software package appropriate for hexagonal close-packed cylindrical pores typical of SBA-15. Mercury intrusion porosimetry was performed using a Quantachrome Poremaster 60 with a 0.5cc penetrometer to determine macropore window size.[64] Sample was inserted into the weighed penetrometer (0.064 g) and the cell filled with mercury at low pressure. The sample was then inserted into the high-pressure chamber and intrusion porosimetry run up to 50000 psi. Data was analysed using Porowin v4.03. Thermogravimetric analysis was conducted using a Mettler-Toledo TGA/DSC 2 STAR* system at 10 ºC min^{-1} under flowing N_2/O_2 (80:20 v/v 20 cm^3 min^{-1}) fitted with a Pfeiffer ThermoStar mass spectrometer.

Powder X-ray diffraction patterns were recorded using a Bruker D8 diffractometer employing a Cu K_α (1.54 Å) source fitted with a Lynx eye high-speed strip detector. Low-angle patterns were recorded for 2θ = 0.3-8º with a step size of 0.01º. Wide-angle patterns were recorded for 2θ = 10-80º with a step size of 0.02º. High-resolution XPS was recorded using a Kratos Axis HSi spectrometer fitted with an Al K_α (1486.6 eV) monochromated source and a charge neutraliser with a pass energy of 40 eV. Dual excitation XPS was recorded using a Kratos SUPRA XPS fitted with monochromated Al (1486.7 eV) and monochromated Ag (2984.3 eV) X-ray sources and an electron flood gun charge neutraliser with a pass energy of 20 eV. Mg 2p XP spectral intensities obtained using monochromated Al K_α (1486.69 eV) versus Ag L_α (2984.3 eV) excitation sources were quantified using inelastic mean free paths of 4.6 and 8.1 nm respectively to assess the vertical distribution of magnesium.[65] All measurements were recorded at a pressure below 10^{-9} Torr. All spectra were calibrated to adventitious carbon (284.8 eV). Peak fitting was performed using CASAv2.3.18PR1.0. All peaks were fit with a Shirley background and a Gaussian-Lorentzian(30) lineshape.

Transmission electron microscopy (TEM) imaging was performed using a JEOL 2100F FEG TEM with a Schottky field-emission source, equipped with an Oxford INCAx-sight Si(Li) detector for energy-dispersive spectroscopy (EDX). High-resolution (scanning) transmission electron microscopy (S)TEM images were recorded on either a FEI Titan^3 Themis G2 operating at 300 kV fitted with 4 EDX silicon drift detectors and

multiple STEM detectors (sub-nm probe size), or a JEOL 2100F FEG STEM operating at 200 kV and equipped with a spherical aberration probe corrector (CEOS GmbH) and a Bruker XFlash 5030 EDX. Samples were prepared for microscopy by dispersion in methanol and drop-casting onto a copper grid coated with a holey carbon support film (Agar Scientific). Images were analysed using ImageJ 1.41 software.

CHNS analysis was performed using a Thermo Flash 2000 CHNS analyser calibrated against a sulphanilamide standard. Samples were prepared in tin capsules using vanadium pentoxide as an accelerant. ICP-OES analysis was performed using a Thermo iCAP 7000 calibrated against a series of standards between 0.1 and 100 ppm. Samples (20 mg) were digested using a CEM SP-D discover microwave in a mixture of ammonium fluoride (100 mg) and nitric acid (5 cm^3) prior to fluoride neutralisation with boric acid (3% solution, 1 cm^3) and hydrochloric acid (1 cm^3). Acid digestion mixtures were diluted to 10 % prior to analysis and measurements were repeated 3 times against 3 distinct wavelengths per element.

Acid/base site characterisation. Brønsted/Lewis acid character was determined from pyridine adsorption by dropping 0.5 cm^3 of pyridine on 10 mg of sample, and subsequent removal of physisorbed pyridine by in vacuo drying at 40 °C/100 mbar in a Heraeus Vacutherm vacuum oven overnight. DRIFT spectra were recorded using a Thermo Nicolet iS50 spectrometer and LN_2 cooled MCT detector, processed using OMNIC 9.2.98 software, and background subtractions using the spectra of untreated parent samples. Relative Brønsted:Lewis character was determined from the ratio of absorbances at 1545-1535 cm^{-1} and 1445 cm^{-1} respectively.[66] Temperature-programmed decomposition of n-propylamine to propene and NH_3 via the Hoffman elimination reaction was used to quantify acid loadings:[67] 0.5 cm^3 of n-propylamine was added to 10 mg of sample, and physisorbed n-propylamine subsequent removed in vacuo by drying at 40 °C/100 mbar in a Heraeus Vacutherm vacuum oven overnight. Thermogravimetric analysis of n-propylamine treated samples was performed under flowing N_2 (20 $cm^3.min^{-1}$) with a ramp rate of 10 °C.min^{-1} using a Mettler-Toledo TGA/DSC 2 STAR* system fitted with a Pfeiffer ThermoStar mass spectrometer. The m/z = 41 signal was monitored to identify the temperature range over which n-propylamine decomposed over acid sites and hence accompanying mass loss over this range and therefore mols of n-propylamine initially adsorbed at acid sites. CO_2 titrations were performed using a Quantachrome ChemBET 3000. Samples were outgassed at 400 ºC under flowing helium (20 cm^3 min^{-1}) for 1

h prior to pulse chemisorption using a fixed volume injection loop. Temperature-programmed desorption (TPD) of CO_2 saturated samples was subsequently performed 10 ºC min^{-1} under flowing He (20 cm^3 min^{-1}) monitoring the m/z = 44 signal.

Low-field NMR relaxation-exchange correlation measurements. Approximately 0.25 g of an unfunctionalised MM-SBA-15 architecture was soaked in excess deionised water (produced onsite at the Australian Resources Research Centre, Perth, Australia) for at least 48 h before analysis. Low-field NMR relaxation data were acquired using an Oxford Instruments Geospec spectrometer equipped with a parallel plate 0.3 T permanent magnet (corresponding to a ^{1}H (proton) NMR frequency of υ_0 = 12.7 MHz) and 53 mm Q-sense probe; all measurements were performed at room temperature (25 ± 2 °C) and under ambient pressure. Both $T_2 - T_2$ and $T_1 - T_2$ correlation measurements were performed; an extensive description of these measurements, together with detailed background theory relating the measured T_1 and T_2 nuclear spin relaxation times to material pore size characteristics, is provided in the **Supplementary Discussion**.

Catalytic testing. Deacetalisation-Knoevenagel cascade reactions were performed in a 25 cm^3 round-bottom flask using a Radleys StarFish reactor with 25 mg of catalyst, 5 mmol BDMA (99 %, Sigma-Aldrich), 50 mmol ethyl cyanoacetate (99 %, Sigma-Aldrich), 5 mmol deionised water, 5 cm^3 toluene (99 %, Sigma-Aldrich) and 1 mmol nonane (99 %, Sigma-Aldrich) as an internal standard. Alternatively, ADMA (98.5 %, Sigma-Aldrich) or FDMA (97 %, Sigma-Aldrich) were used instead of BDMA. Knoevenagel condensation was performed using 5 mmol benzaldehyde (99 %, Sigma-Aldrich) instead of BMDA, and in the presence of 5 mmol deionised water to mirror the cascade reaction conditions (wherein water is required to hydrolyse the C-O bond in BDMA in the first step). Reactions were performed at 50 °C under a N_2 atmosphere. 0.25 cm^3 aliquots were periodically sampled, filtered to remove catalyst, diluted with toluene, and analysed by gas chromatography using a Varian 450 GC and ZB-5 column (30 m x 0.53 mm x 1.50 μm). Average rates were calculated over the first 10 min of reaction.

Esterification, transesterification, and simultaneous esterification/transesterification reactions over hierarchical porous catalysts were performed in a 100 cm^3 ACE round-bottom pressure flask, fitted with a

sampling dip-tube, using 25 mg of catalyst in 60 cm^3 methanol and 0.1 mmol dihexylether as an internal standard (99 %, Sigma-Aldrich) and either 5 mmol tributyrin (98 %, Fisher) 5 mmol hexanoic acid (99 %, Sigma-Aldrich) or a mixture of 5 mmol tributyrin and 5 mmol hexanoic acid. Reactions were performed at 90 °C under air at autogeneous pressure. 1 cm^3 aliquots were periodically sampled, filtered to remove catalyst, and analysed by gas chromatography using a Varian 3800 GC and ZB-50 column (30 m x 0.25 mm x 0.25 μm). Average rates were calculated over the first 30 min of reaction.

Transesterification and simultaneous esterification/transesterification reactions over MgO/SZ and SZ nanoparticle catalysts were performed in 100 cm^3 2 neck round-bottom flasks fitted with Findensers and suba-seal septa. Flasks were charged with 100 mg of catalyst in 60 cm^3 methanol (Univar, 99.8 %) and 0.1 mmol dihexylether as an internal standard (99 %, Sigma-Aldrich), and either 5 mmol tributyrin (Aldrich 98.5 %) or a mixture of 5 mmol tributyrin and 5 mmol hexanoic acid Aldrich 99 %). Reactions were performed at 60 °C under air with 500 rpm of agitation using a 25 mm stirrer bar. 0.5 cm^3 aliquots were periodically sampled, filtered to remove catalyst, and analysed by gas chromatography using a Perkin Elmer Clarus 590 GC and ZB-1HT column (30 m x 0.32 mm x 0.1 μm).

Data availability

The data that support the findings of this study are available from the corresponding author upon reasonable request.

References

1. Climent, M. J., Corma, A. & Iborra, S. Heterogeneous catalysts for the one-pot synthesis of chemicals and fine chemicals. *Chem. Rev.* **111**, 1072-1133 (2010).
2. Climent, M. J., Corma, A. & Iborra, S. Homogeneous and heterogeneous catalysts for multicomponent reactions. *RSC Adv.* **2**, 16-58 (2012).
3. Kulkarni, M. G. & Dalai, A. K. Waste Cooking OilAn Economical Source for Biodiesel: A Review. *Ind. Eng. Chem. Res.* **45**, 2901-2913 (2006).
4. Biju, A. T., Wurz, N. E. & Glorius, F. N-heterocyclic carbene-catalyzed cascade reaction involving the hydroacylation of unactivated alkynes. *J. Am. Chem. Soc.* **132**, 5970-5971 (2010).
5. Enders, D., Huettl, M. R., Grondal, C. & Raabe, G. Control of four stereocentres in a triple cascade organocatalytic reaction. *Nature* **441**, 861-863 (2006).
6. Climent, M. J., Corma, A., Iborra, S. & Sabater, M. J. Heterogeneous Catalysis for Tandem Reactions. *ACS Catal.* **4**, 870-891 (2014).

7. Fraile, J. M., Mallada, R., Mayoral, J. A., Menéndez, M. & Roldán, L. Shift of Multiple Incompatible Equilibriums by a Combination of Heterogeneous Catalysis and Membranes. *Chem. Eur. J.* **16**, 3296-3299 (2010).
8. Wheeldon, I. *et al.* Substrate channelling as an approach to cascade reactions. *Nat. Chem.* **8**, 299 (2016).
9. Fogg, D. E. & dos Santos, E. N. Tandem catalysis: a taxonomy and illustrative review. *Coord. Chem. Rev.* **248**, 2365-2379 (2004).
10. Li, L. & Herzon, S. B. Temporal separation of catalytic activities allows anti-Markovnikov reductive functionalization of terminal alkynes. *Nat. Chem.* **6**, 22 (2013).
11. Lohr, T. L. & Marks, T. J. Orthogonal tandem catalysis. *Nat. Chem.* **7**, 477-482 (2015).
12. Singh, N. *et al.* Tandem reactions in self-sorted catalytic molecular hydrogels. *Chem. Sci.* **7**, 5568-5572 (2016).
13. Zeidan, R. K., Hwang, S.-J. & Davis, M. E. Multifunctional Heterogeneous Catalysts: SBA-15-Containing Primary Amines and Sulfonic Acids. *Angew. Chem. Int. Ed.* **45**, 6332-6335 (2006).
14. Brunelli, N. A., Venkatasubbaiah, K. & Jones, C. W. Cooperative Catalysis with Acid–Base Bifunctional Mesoporous Silica: Impact of Grafting and Co-condensation Synthesis Methods on Material Structure and Catalytic Properties. *Chem. Mater.* **24**, 2433-2442 (2012).
15. Gianotti, E., Diaz, U., Velty, A. & Corma, A. Designing bifunctional acid–base mesoporous hybrid catalysts for cascade reactions. *Catal. Sci. Technol.* **3**, 2677-2688 (2013).
16. Weng, Z., Yu, T. & Zaera, F. Synthesis of Solid Catalysts with Spatially Resolved Acidic and Basic Molecular Functionalities. *ACS Catal.* **8**, 2870-2879 (2018).
17. Corma, A., Díaz, U., García, T., Sastre, G. & Velty, A. Multifunctional hybrid organic− inorganic catalytic materials with a hierarchical system of well-defined micro-and mesopores. *J. Am. Chem. Soc.* **132**, 15011-15021 (2010).
18. Bass, J. D. & Katz, A. Bifunctional Surface Imprinting of Silica: Thermolytic Synthesis and Characterization of Discrete Thiol−Amine Functional Group Pairs. *Chem. Mater.* **18**, 1611-1620 (2006).
19. Yu, X. *et al.* The effect of the distance between acidic site and basic site immobilized on mesoporous solid on the activity in catalyzing aldol condensation. *J. Solid State Chem.* **184**, 289-295 (2011).
20. Margelefsky, E. L., Bendjériou, A., Zeidan, R. K., Dufaud, V. & Davis, M. E. Nanoscale Organization of Thiol and Arylsulfonic Acid on Silica Leads to a Highly Active and Selective Bifunctional, Heterogeneous Catalyst. *J. Am. Chem. Soc.* **130**, 13442-13449 (2008).
21. Margelefsky, E. L., Zeidan, R. K. & Davis, M. E. Cooperative catalysis by silica-supported organic functional groups. *Chem. Soc. Rev.* **37**, 1118-1126 (2008).
22. Gao, J., Zhang, X., Lu, Y., Liu, S. & Liu, J. Selective Functionalization of Hollow Nanospheres with Acid and Base Groups for Cascade Reactions. *Chem. Eur. J.* **21**, 7403-7407 (2015).
23. Merino, E. *et al.* Synthesis of structured porous polymers with acid and basic sites and their catalytic application in cascade-type reactions. *Chem. Mater.* **25**, 981-988 (2013).
24. Li, P. *et al.* Core–shell structured mesoporous silica as acid–base bifunctional catalyst with designated diffusion path for cascade reaction sequences. *Chem. Commun.* **48**, 10541-10543 (2012).
25. Li, P. *et al.* Core-shell structured MgAl-LDO@Al-MS hexagonal nanocomposite: an all inorganic acid-base bifunctional nanoreactor for one-pot cascade reactions. *J. Mater. Chem. A* **2**, 339-344 (2014).
26. Vernekar, D. & Jagadeesan, D. Tunable acid-base bifunctional catalytic activity of FeOOH in an orthogonal tandem reaction. *Catal. Sci. Technol.* **5**, 4029-4038 (2015).
27. Huang, Y., Xu, S. & Lin, V. S. Y. Bifunctionalized Mesoporous Materials with Site-Separated Brønsted Acids and Bases: Catalyst for a Two-Step Reaction Sequence. *Angew. Chem.* **123**, 687-690 (2011).
28. Yang, Y. *et al.* A Yolk–Shell Nanoreactor with a Basic Core and an Acidic Shell for Cascade Reactions. *Angew. Chem. Int. Ed.* **51**, 9164-9168 (2012).
29. Jun, S. W. *et al.* One-pot synthesis of magnetically recyclable mesoporous silica supported acid–base catalysts for tandem reactions. *Chem. Commun.* **49**, 7821-7823 (2013).
30. Motokura, K. *et al.* An acidic layered clay is combined with a basic layered clay for one-pot sequential reactions. *J. Am. Chem. Soc.* **127**, 9674-9675 (2005).
31. Corma, A. Inorganic Solid Acids and Their Use in Acid-Catalyzed Hydrocarbon Reactions. *Chem. Rev.* **95**, 559-614 (1995).
32. Choudary, B. M., Ranganath, K. V., Pal, U., Kantam, M. L. & Sreedhar, B. Nanocrystalline MgO for asymmetric Henry and Michael reactions. *J. Am. Chem. Soc.* **127**, 13167-13171 (2005).

33. Díez, V., Apesteguía, C. & Di Cosimo, J. Aldol condensation of citral with acetone on MgO and alkali-promoted MgO catalysts. *J. Catal.* **240**, 235-244 (2006).
34. Shimizu, K.-i. & Satsuma, A. Toward a rational control of solid acid catalysis for green synthesis and biomass conversion. *Energy Environ. Sci.* **4**, 3140-3153 (2011).
35. Osatiashtiani, A., Durndell, L. J., Manayil, J. C., Lee, A. F. & Wilson, K. Influence of alkyl chain length on sulfated zirconia catalysed batch and continuous esterification of carboxylic acids by light alcohols. *Green Chem.* **18**, 5529-5535 (2016).
36. Montero, J. M., Gai, P., Wilson, K. & Lee, A. F. Structure-sensitive biodiesel synthesis over MgO nanocrystals. *Green Chem.* **11**, 265-268 (2009).
37. Ciddor, L., Bennett, J. A., Hunns, J. A., Wilson, K. & Lee, A. F. Catalytic upgrading of bio-oils by esterification. *J. Chem. Technol. Biotechnol.* **90**, 780-795 (2015).
38. Chai, M., Tu, Q., Lu, M. & Yang, Y. J. Esterification pretreatment of free fatty acid in biodiesel production, from laboratory to industry. *Fuel Process. Technol.* **125**, 106-113 (2014).
39. Xu, P.-F. & Wang, W. *Catalytic Cascade Reactions*. (John Wiley & Sons, 2013).
40. Djakovitch, L., Dufaud, V. & Zaidi, R. Heterogeneous Palladium Catalysts Applied to the Synthesis of 2- and 2,3-Functionalised Indoles. *Adv. Synth. Catal.* **348**, 715-724 (2006).
41. Peng, W.-H., Lee, Y.-Y., Wu, C. & Wu, K. C. W. Acid–base bi-functionalized, large-pored mesoporous silica nanoparticles for cooperative catalysis of one-pot cellulose-to-HMF conversion. *J. Mater. Chem.* **22**, 23181-23185 (2012).
42. Takagaki, A., Ohara, M., Nishimura, S. & Ebitani, K. A one-pot reaction for biorefinery: combination of solid acid and base catalysts for direct production of 5-hydroxymethylfurfural from saccharides. *Chem. Commun.*, 6276-6278 (2009).
43. Shiju, N. R., Alberts, A. H., Khalid, S., Brown, D. R. & Rothenberg, G. Mesoporous Silica with Site-Isolated Amine and Phosphotungstic Acid Groups: A Solid Catalyst with Tunable Antagonistic Functions for One-Pot Tandem Reactions. *Angew. Chem. Int. Ed.* **50**, 9615-9619 (2011).
44. Shiju, N. R., Alberts, A. H., Khalid, S., Brown, D. R. & Rothenberg, G. Mesoporous Silica with Site-Isolated Amine and Phosphotungstic Acid Groups: A Solid Catalyst with Tunable Antagonistic Functions for One-Pot Tandem Reactions. *Angew. Chem.* **123**, 9789-9793 (2011).
45. Cohen, B. J., Kraus, M. A. & Patchornik, A. "Wolf and Lamb" reactions equilibrium and kinetic effects in multipolymer systems. *J. Am. Chem. Soc.* **103**, 7620-7629 (1981).
46. Chi, Y., Scroggins, S. T. & Fréchet, J. M. J. One-Pot Multi-Component Asymmetric Cascade Reactions Catalyzed by Soluble Star Polymers with Highly Branched Non-Interpenetrating Catalytic Cores. *J. Am. Chem. Soc.* **130**, 6322-6323 (2008).
47. Parlett, C. M. *et al.* Spatially orthogonal chemical functionalization of a hierarchical pore network for catalytic cascade reactions. *Nat. Mater.* **15**, 178-182 (2016).
48. Wei, Y. L., Wang, Y. M., Zhu, J. H. & Wu, Z. Y. In-Situ Coating of SBA-15 with MgO: Direct Synthesis of Mesoporous Solid Bases from Strong Acidic Systems. *Adv. Mater.* **15**, 1943-1945 (2003).
49. Osatiashtiani, A. *et al.* Hydrothermally stable, conformal, sulfated zirconia monolayer catalysts for glucose conversion to 5-HMF. *ACS Catal.* **5**, 4345-4352 (2015).
50. Zhang, Y., Liang, H., Zhao, C. Y. & Liu, Y. Macroporous alumina monoliths prepared by filling polymer foams with alumina hydrosols. *J. Mater. Sci.* **44**, 931-938 (2009).
51. Di Cosimo, J. I., Diez, V. K., Ferretti, C. & Apesteguia, C. R. in *Catalysis: Volume 26* Vol. 26 1-28 (The Royal Society of Chemistry, 2014).
52. Pennycook, S. & Boatner, L. Chemically sensitive structure-imaging with a scanning transmission electron microscope. *Nature* **336**, 565 (1988).
53. Robinson, N., Robertson, C., Gladden, L. F., Jenkins, S. J. & D'Agostino, C. Direct Correlation between Adsorption Energetics and Nuclear Spin Relaxation in a Liquid-saturated Catalyst Material. *ChemPhysChem* **19**, 2472-2479 (2018).
54. Isaacs, M. A. *et al.* Unravelling mass transport in hierarchically porous catalysts. *J. Mater. Chem. A* **7**, 11814-11825 (2019).
55. Robinson, N. & D'Agostino, C. NMR Investigation into the Influence of Surface Interactions on Liquid Diffusion in a Mesoporous Catalyst Support. *Top. Catal.* **63**, 391-327 (2020).
56. Song, Y. Q. *et al.* T1–T2 Correlation Spectra Obtained Using a Fast Two-Dimensional Laplace Inversion. *J. Magn. Reson.* **154**, 261-268 (2002).

57. Galarneau, A., Cambon, H., Di Renzo, F. & Fajula, F. True Microporosity and Surface Area of Mesoporous SBA-15 Silicas as a Function of Synthesis Temperature. *Langmuir* **17**, 8328-8335 (2001).
58. Mitchell, J. *et al.* Validation of NMR relaxation exchange time measurements in porous media. *J. Chem. Phys.* **127**, 234701 (2007).
59. Li, G., Xiao, J. & Zhang, W. Efficient and reusable amine-functionalized polyacrylonitrile fiber catalysts for Knoevenagel condensation in water. *Green Chem.* **14**, 2234-2242 (2012).
60. Chen, X., Arruebo, M. & Yeung, K. L. Flow-synthesis of mesoporous silicas and their use in the preparation of magnetic catalysts for Knoevenagel condensation reactions. *Catal. Today* **204**, 140-147 (2013).
61. Sen, T., Tiddy, G., Casci, J. & Anderson, M. Synthesis and characterization of hierarchically ordered porous silica materials. *Chem. Mater.* **16**, 2044-2054 (2004).
62. Wainwright, S. G. *et al.* True liquid crystal templating of SBA-15 with reduced microporosity. *Micropor. Mesopor. Mat.* **172**, 112-117 (2013).
63. Mazumder, V. & Sun, S. Oleylamine-mediated synthesis of Pd nanoparticles for catalytic formic acid oxidation. *J. Am. Chem. Soc.* **131**, 4588-4589 (2009).
64. Brun, N. *et al.* Hard macrocellular silica Si (HIPE) foams templating micro/macroporous carbonaceous monoliths: applications as lithium ion battery negative electrodes and electrochemical capacitors. *Adv. Funct. Mater.* **19**, 3136-3145 (2009).
65. Akkerman, A. *et al.* Inelastic electron interactions in the energy range 50 eV to 10 keV in insulators: Alkali halides and metal oxides. *Phys. Status Solidi B* **198**, 769-784 (1996).
66. Platon, A. & Thomson, W. J. Quantitative Lewis/Brönsted Ratios Using DRIFTS. *Ind. Eng. Chem. Res.* **42**, 5988-5992 (2003).
67. Farneth, W. E. & Gorte, R. J. Methods for Characterizing Zeolite Acidity. *Chem. Rev.* **95**, 615-635 (1995).

Acknowledgements

Support from the Australian Research Council (LP180100116, IC150100019, DP 200100204 and DP200100313) is gratefully acknowledged. Electron microscopy access was provided through the Leeds EPSRC Nanoscience and Nanotechnology Research Equipment Facility (LENNF) (EP/K023853/1), the University of Birmingham Nanoscale Physics Laboratory, and DU GJ Russell Microscopy Facility.

Author contributions

A.F.L. and K.W. conceived the work. A.F.L. M.A.I., C.M.A.P. and K.W. planned the experiments. M.A.I. and A.C.L. synthesised materials. S.K.B. and S.J. synthesised Pt nanoparticles. M.A.I., A.C.L. and J.M. performed catalytic testing. M.A.I., C.M.A.P., L.J.D., N.S.H., D.J. and N.R. undertook materials characterisation. N.R. and M.L.J. analysed NMR data. M.A.I., C.M.A.P., N.R., M.L.J., K.W. and A.F.L. wrote the manuscript.

Competing Interest

The authors declare no competing interests.

Additional information

Extended data is available for this paper at

Supplementary information is available for this paper at

Correspondence and requests for materials should be addressed to A.F.L..

Figure 1: **Substrate channelling in hierarchical pore networks.** Limitations of conventional versus spatially orthogonal approaches to catalytic cascades; the latter affords intrinsic control over the reaction sequence and prevents negative interactions between (e.g. chemically incompatible) active sites.

Figure 2: Synthetic route to a spatially orthogonal, acid-base hierarchically porous framework. **a**, A P123-templated silica mesophase containing Mg^{2+} cations is formed around an ordered array of polystyrene colloidal nanospheres. **b**, Polystyrene hard template is extracted to form a macropore network. **c**, A $Zr(OH)_x$ conformal adlayer is deposited throughout the macropores. **d**, Sulfation of $Zr(OH)_x$ conformal adlayer. **e**, Calcination to remove P123 soft template, and form MgO nanoparticles (NPs) entrained within mesopores and a SZ adlayer selectively coating macropores.

Figure 3: Spatial distribution of Mg and Zr within hierarchically porous SBA-15 framework. **a**, HAADF-STEM image exhibiting bright macropore perimeters. **b**, EDX linescan across a mesopore domain bound by macropores. **c**, HAADF-STEM image of a single mesopore region bound by macropores. **d**, Superposition of EDX elemental maps for image **c** with macropore and mesopore domains indicated. **e**, Elemental quantification of Mg and Zr distribution across image **d**. **f**, Area averaged Zr:Mg atomic ratio within macropore and mesopore domains indicated in **d**.

Figure 4: Antagonistic reactions in biodiesel production. (a) base catalysed transesterification of tributyrin with methanol, and (b) acid catalysed esterification of hexanoic acid to FAME.

Figure 5: Substrate channelling: esterification and transesterification over acid/base catalysts. **a**, Average rate of tributyrin transesterification over SZ/MgO/MM-SBA-15, a 1:1 by weight physical mixture of MgO/MM-SBA-15 and SZ/MM-SBA-15, or MgO/MM-SBA-15, in the absence and

presence of hexanoic acid. **b**, Schematic of proposed substrate channelling mechanism: (i) TAG+FFA mixture enters macropores; (ii) FFA undergoes esterification over SZ (**A**cid) sites and is neutralised in macropores; unreacted TAG diffuses and undergoes transesterification over MgO (**B**ase) sites within mesopores. Reaction conditions: 25 mg of catalyst (except for physical mixture where 25 mg of each monofunctional catalyst was used), 5 mmol tributyrin (or 5 mmol hexanoic acid, or a mixture of 5 mmol tributyrin and 5 mmol hexanoic acid), 60 cm^3 methanol, 0.1 mmol dihexylether as an internal standard, 90 °C under air (autogenous pressure). Error bars represent S.D. of the mean (n=3).

Figure 6: NMR relaxation-exchange correlation data. a-d, Low-field ^1H relaxation-exchange correlation plots for water in unfunctionalised MM-SBA-15 with various t_{mix} times. Normalised peak intensities are defined by the colour bars, which follow a linear scale. On-diagonal peaks A, B, C and D are assigned to water populations: (A) outside the hierarchical pore framework, (B) within macropores, (C) within mesopores, and (D) within micropores, while off-diagonal cross-peaks indicate diffusive-exchange between these sites on the time-scale of t_{mix}. The reduction in peak resolution at short T_2 arises from longitudinal (T_1) relaxation processes during t_{mix}.

Figure 7: **Cascade deacetalisation and Knoevenagel condensation over acid/base catalysts. a,** acid catalysed deactalisation of BDMA to BZALD and subsequent base catalysed Knoevenagel condensation to BCA. **b**, BDMA conversion and BCA yield from BDMA after 6 h reaction over SZ/MgO/MM-SBA-15, SZ/MM-SBA-15, MgO/MM-SBA-15, a 1:1 by weight physical mixture of SZ/MM-SBA-15 and MgO/MM-SBA-15, or without catalyst. **c**, Benzaldehyde (BZALD) conversion and BCA yield after 6 h reaction over SZ/MgO/MM-SBA-15, SZ/MM-SBA-15, MgO/MM-SBA-15, a 1:1 by weight physical mixture of SZ/MM-SBA-15 and MgO/MM-SBA-15, or without catalyst. Reaction conditions: 25 mg of catalyst (except for physical mixture where 25 mg of each monofunctional catalyst was used), 5 mmol BDMA or BZALD, 50 mmol ethyl cyanoacetate, 5 mmol

deionised water, 5 cm^3 toluene, 1 mmol nonane as an internal standard, 50 °C under N_2. Error bars represent S.D. of the mean (n=2).

Conventional approach:
- bifunctional catalyst, random active sites
- physical mix of two monofunctional catalysts

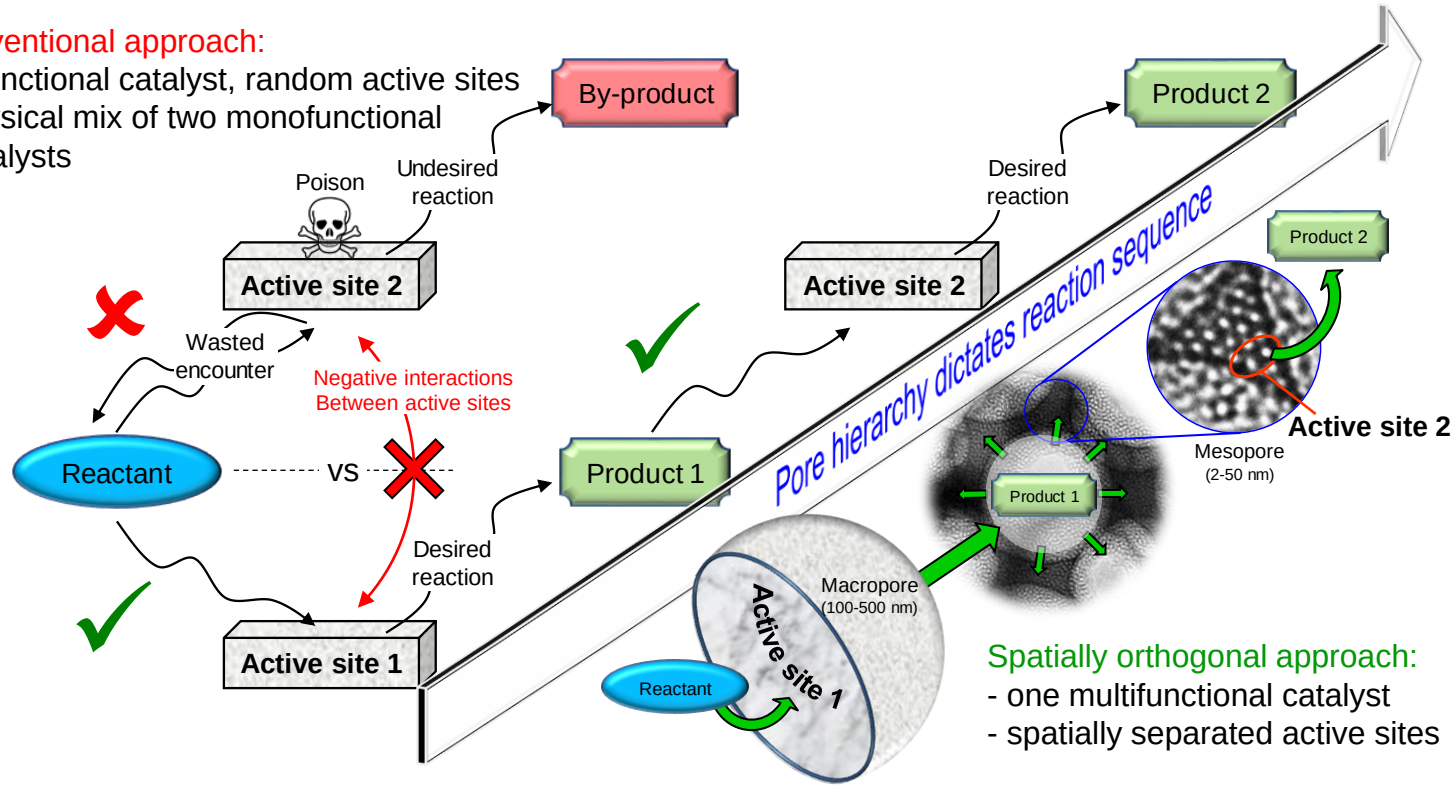

Spatially orthogonal approach:
- one multifunctional catalyst
- spatially separated active sites

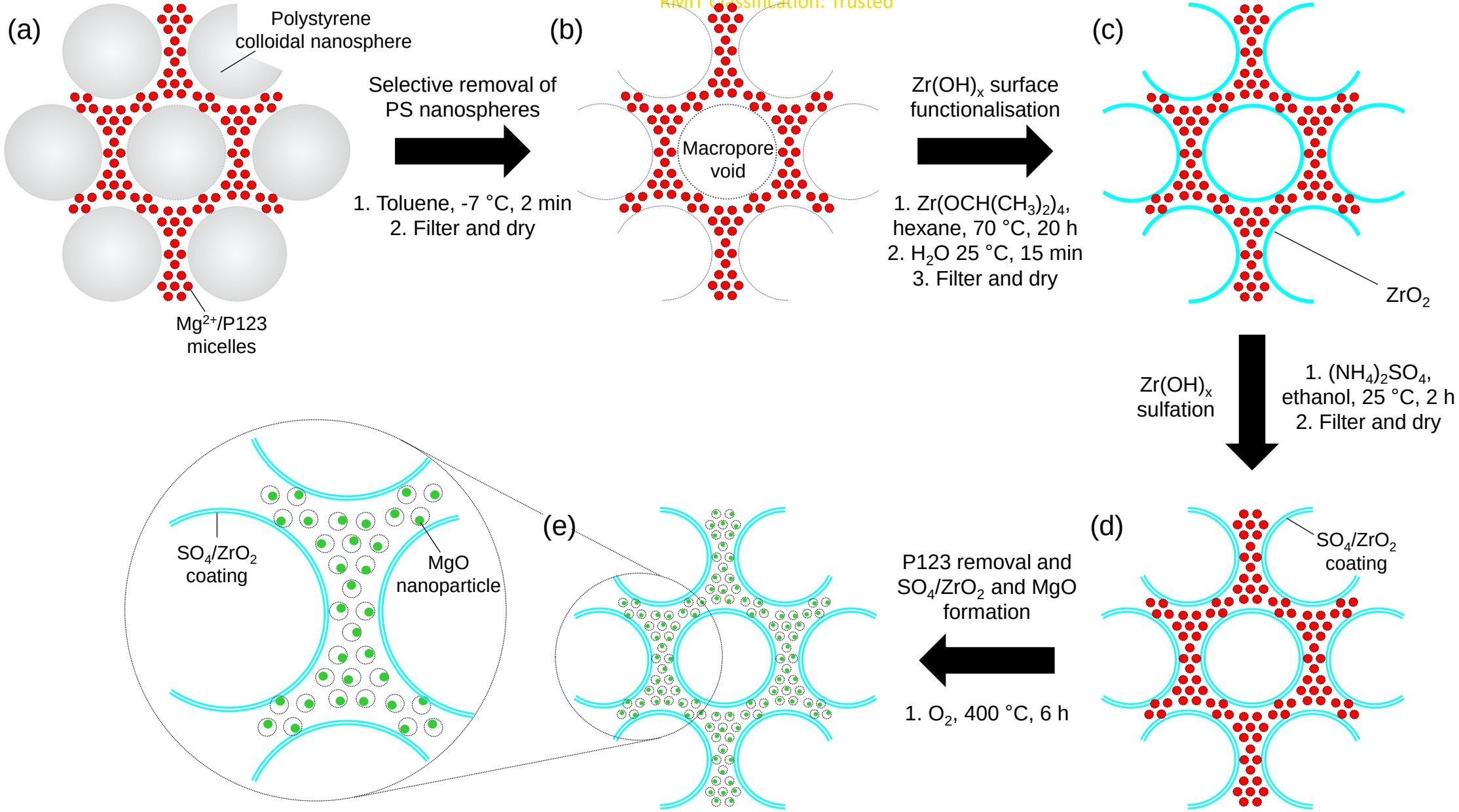

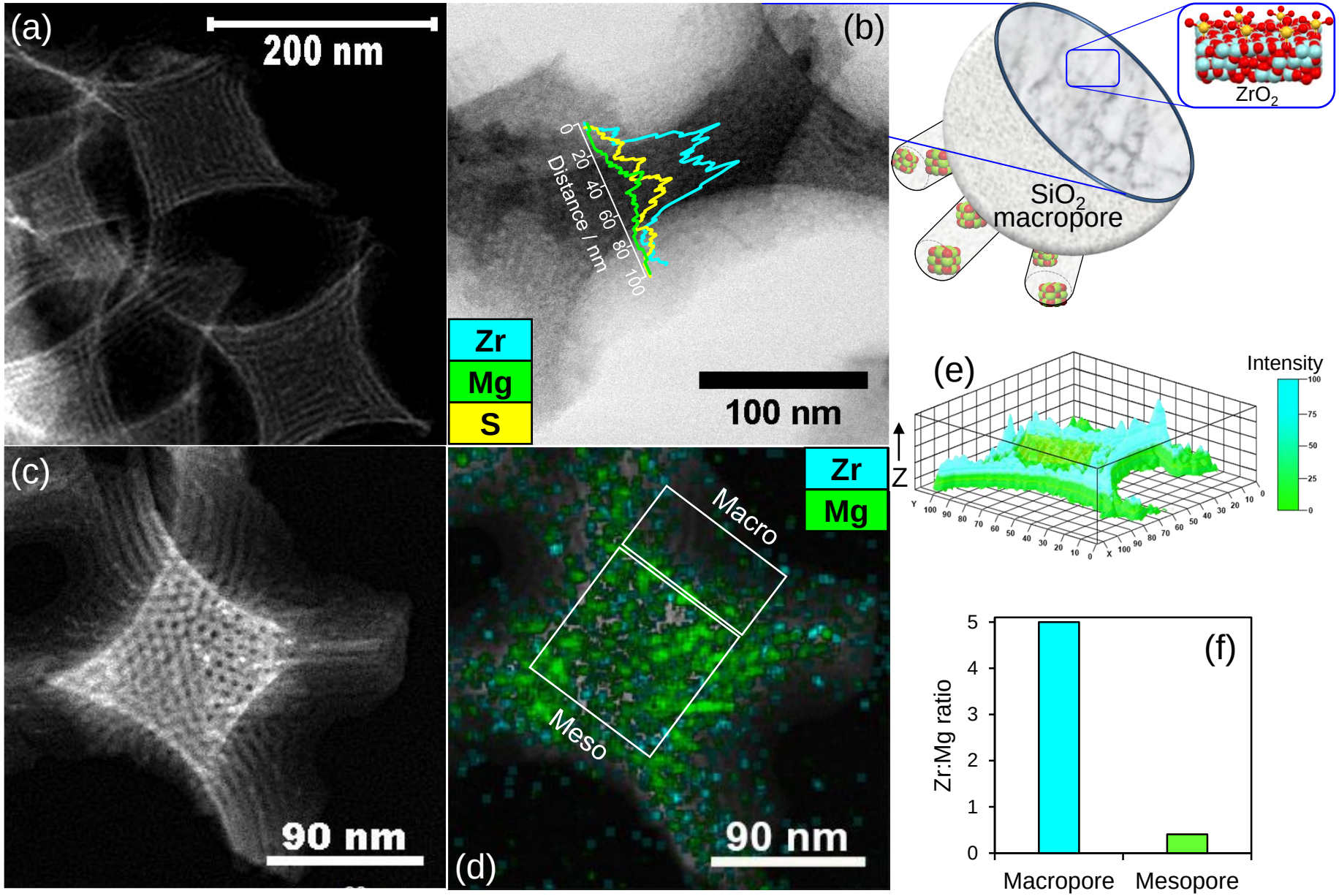

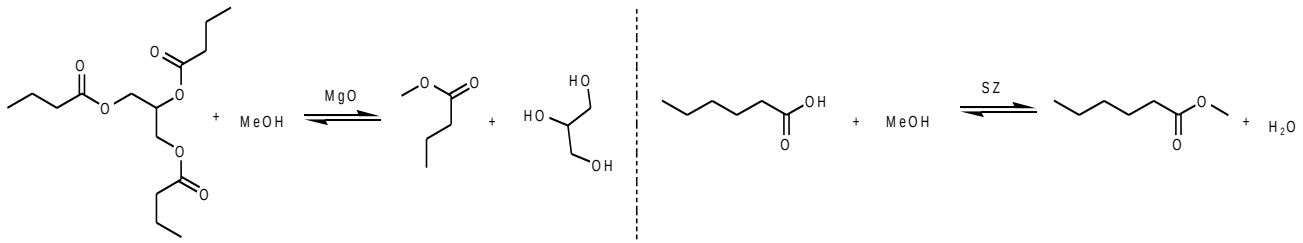
MgO
MeOH
SZ
MeOH
H_2O

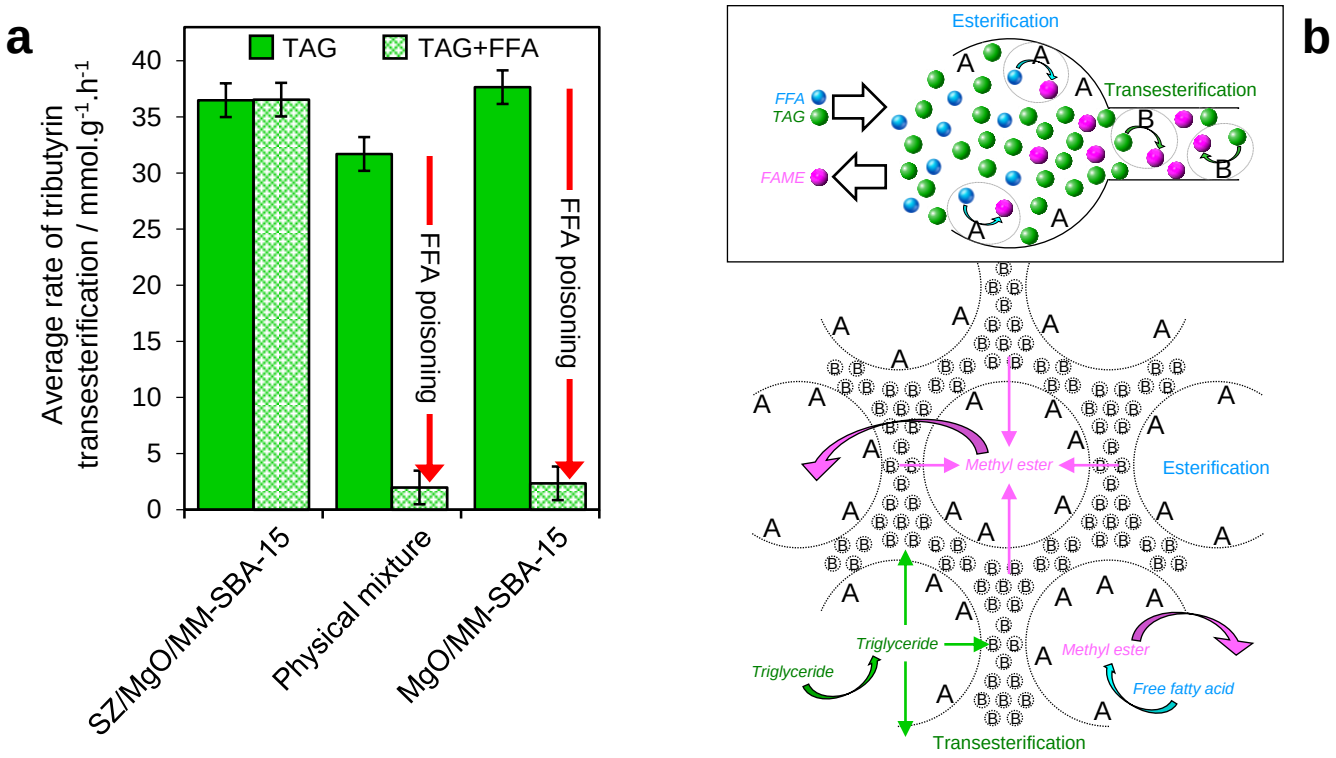
a
TAG
TAG+FFA
Average rate of tributyrin transesterification / mmol.g-1.h-1
40
35
30
25
20
15
10
5
0
FFA poisoning
FFA poisoning
SZ/MgO/MM-SBA-15
Physical mixture
MgO/MM-SBA-15
b
Esterification
FFA
TAG
FAME
Transesterification
Methyl ester
Esterification
Triglyceride
Triglyceride
Methyl ester
Free fatty acid
Transesterification

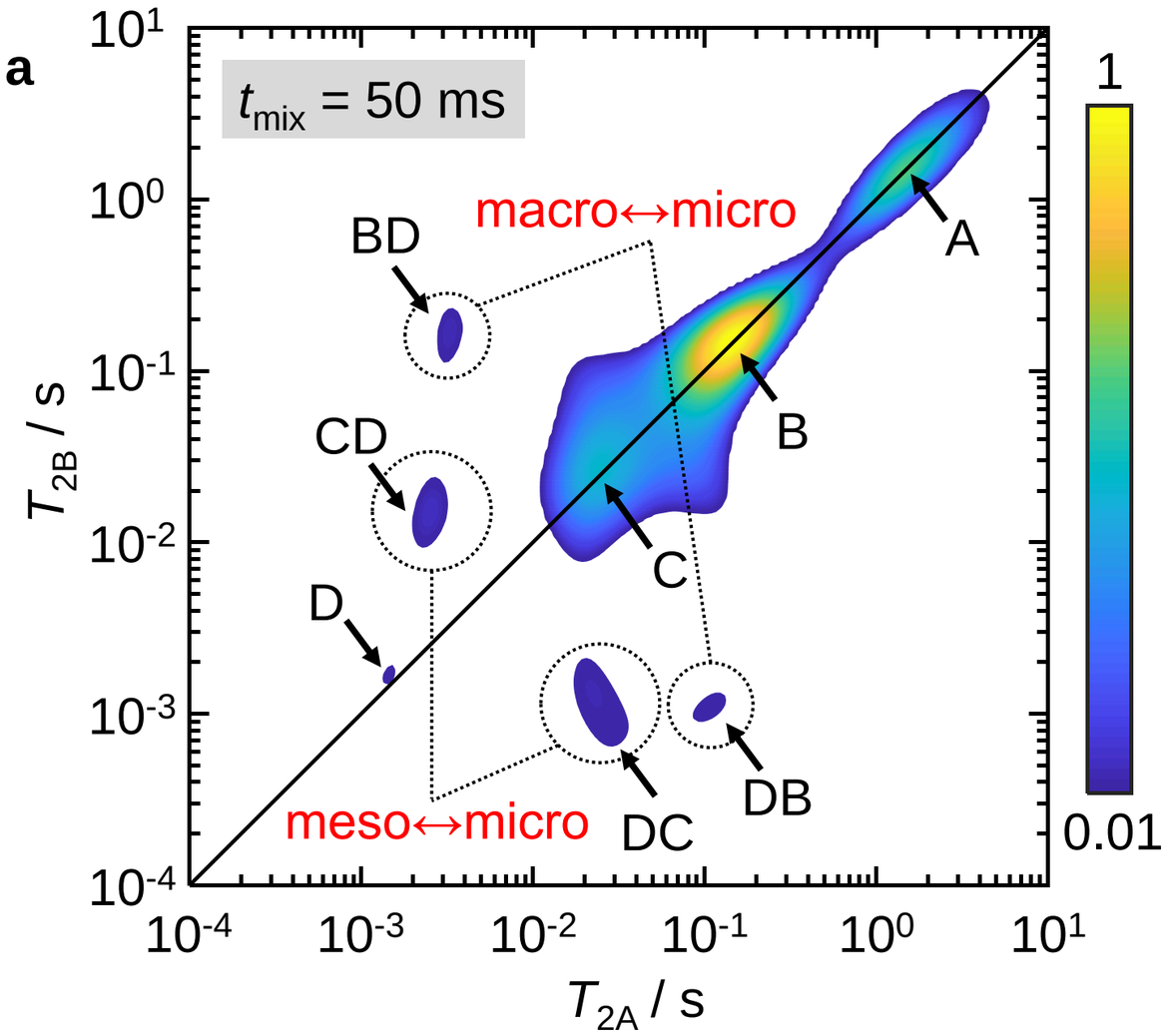

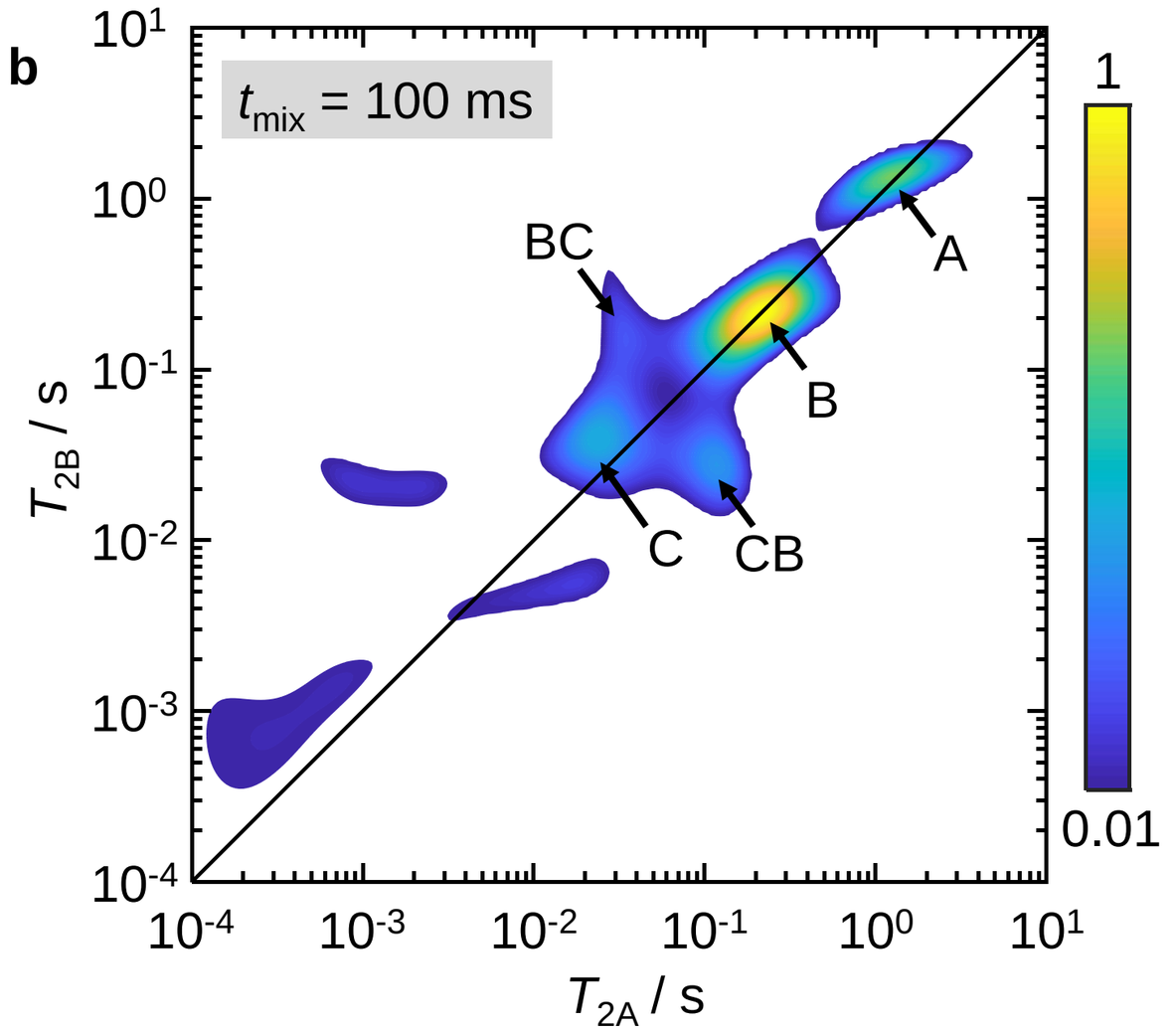

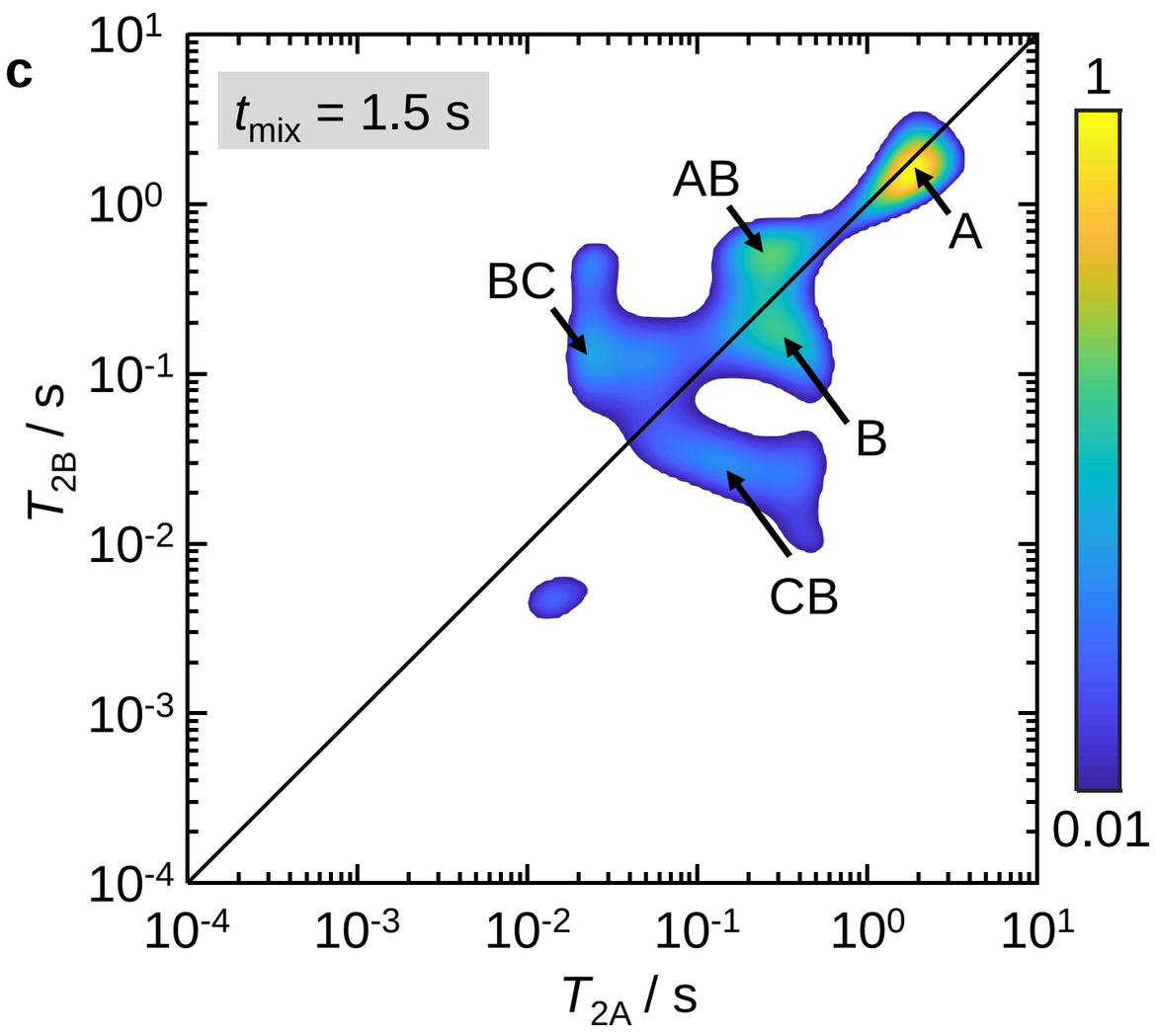

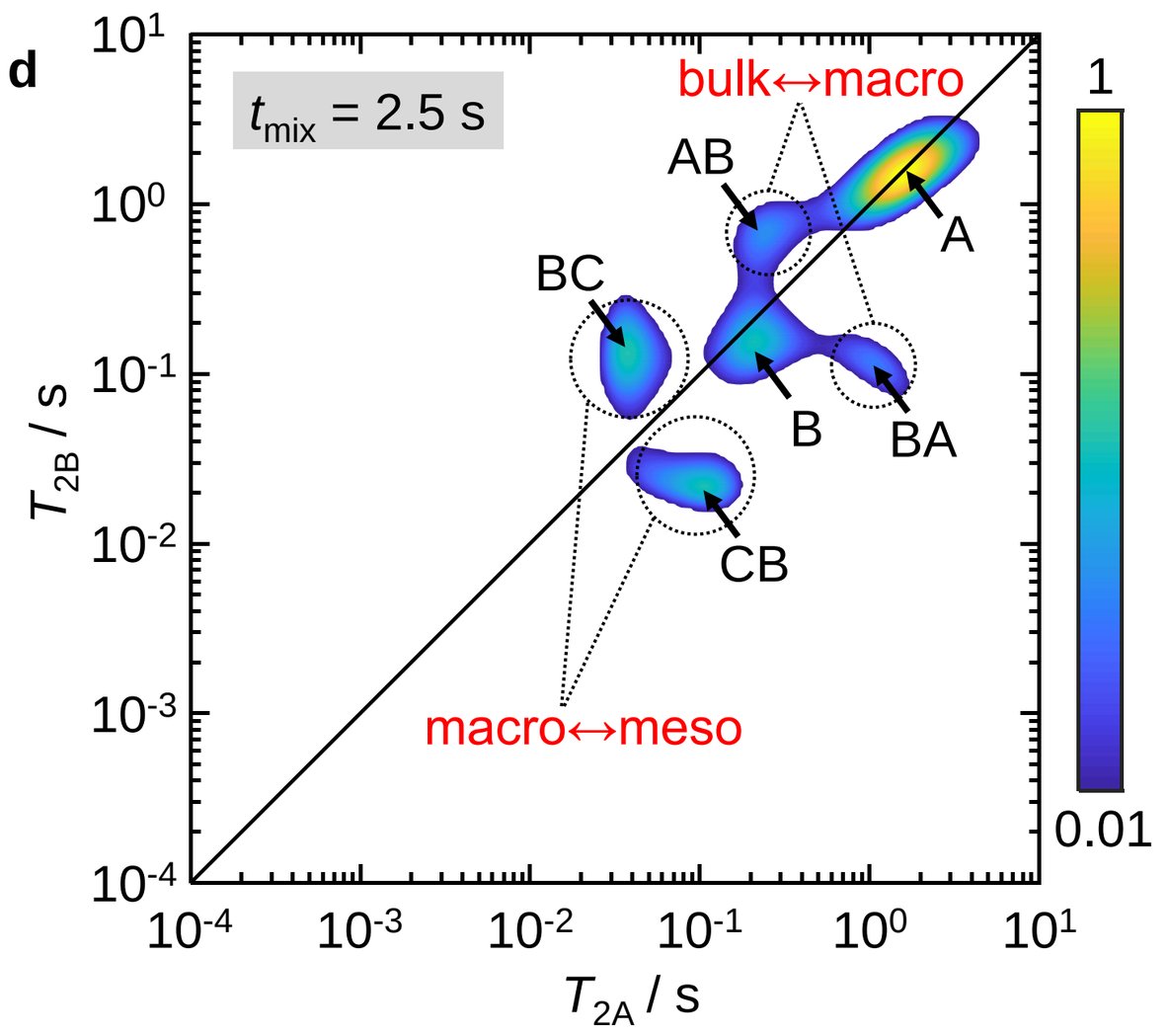

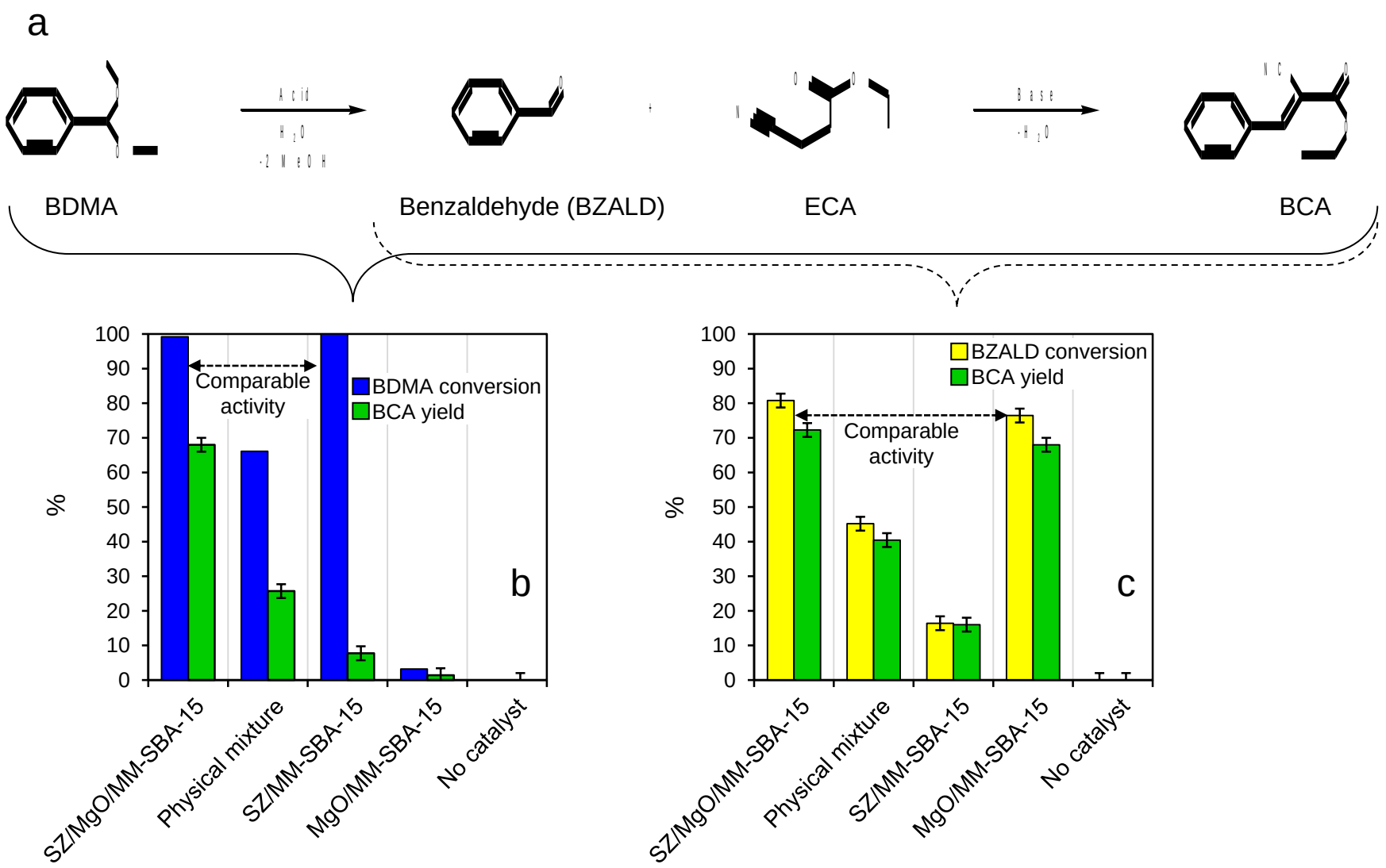

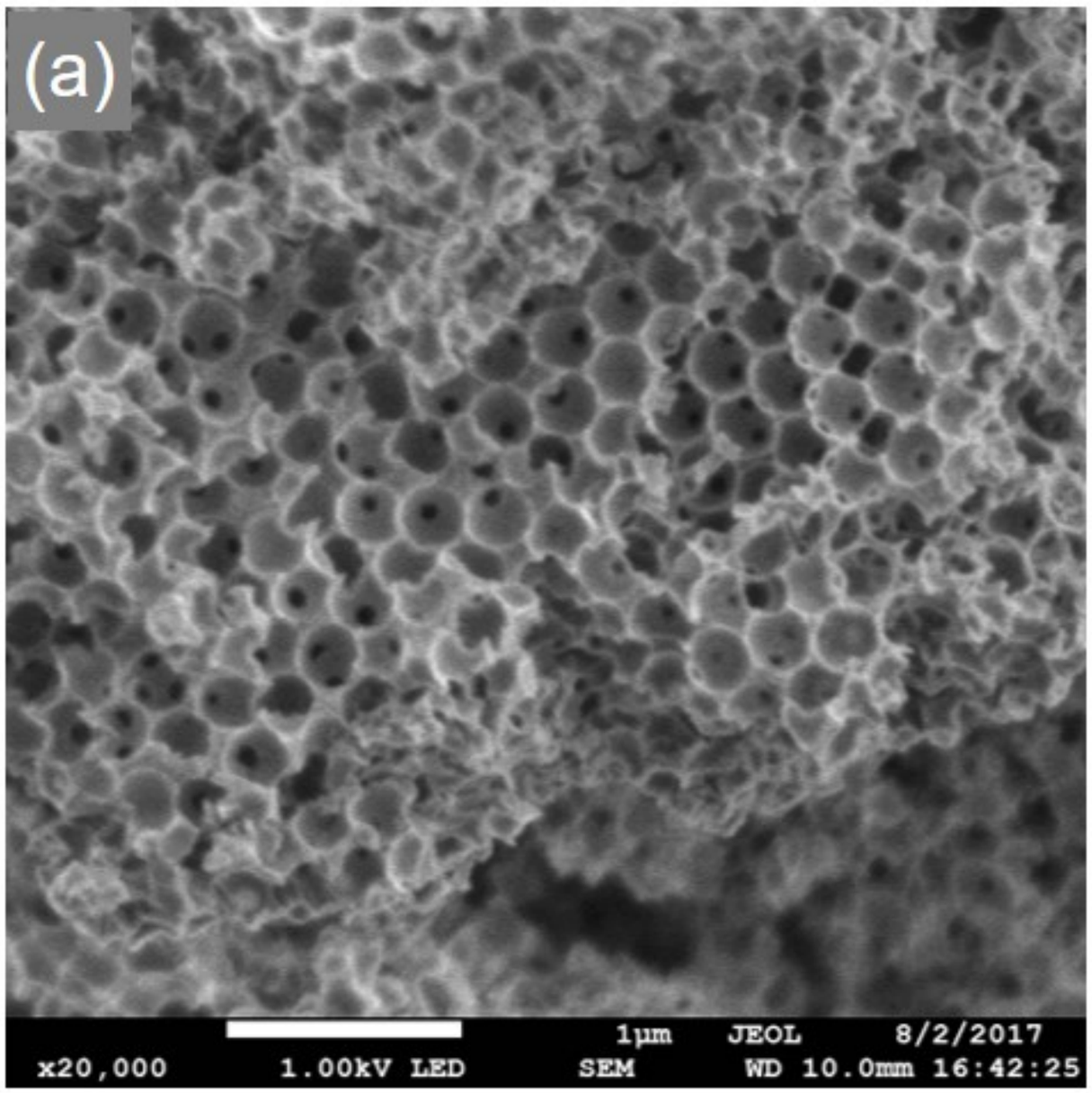
(a)
1µm JEOL 8/2/2017
x20,000 1.00kV LED SEM WD 10.0mm 16:42:25

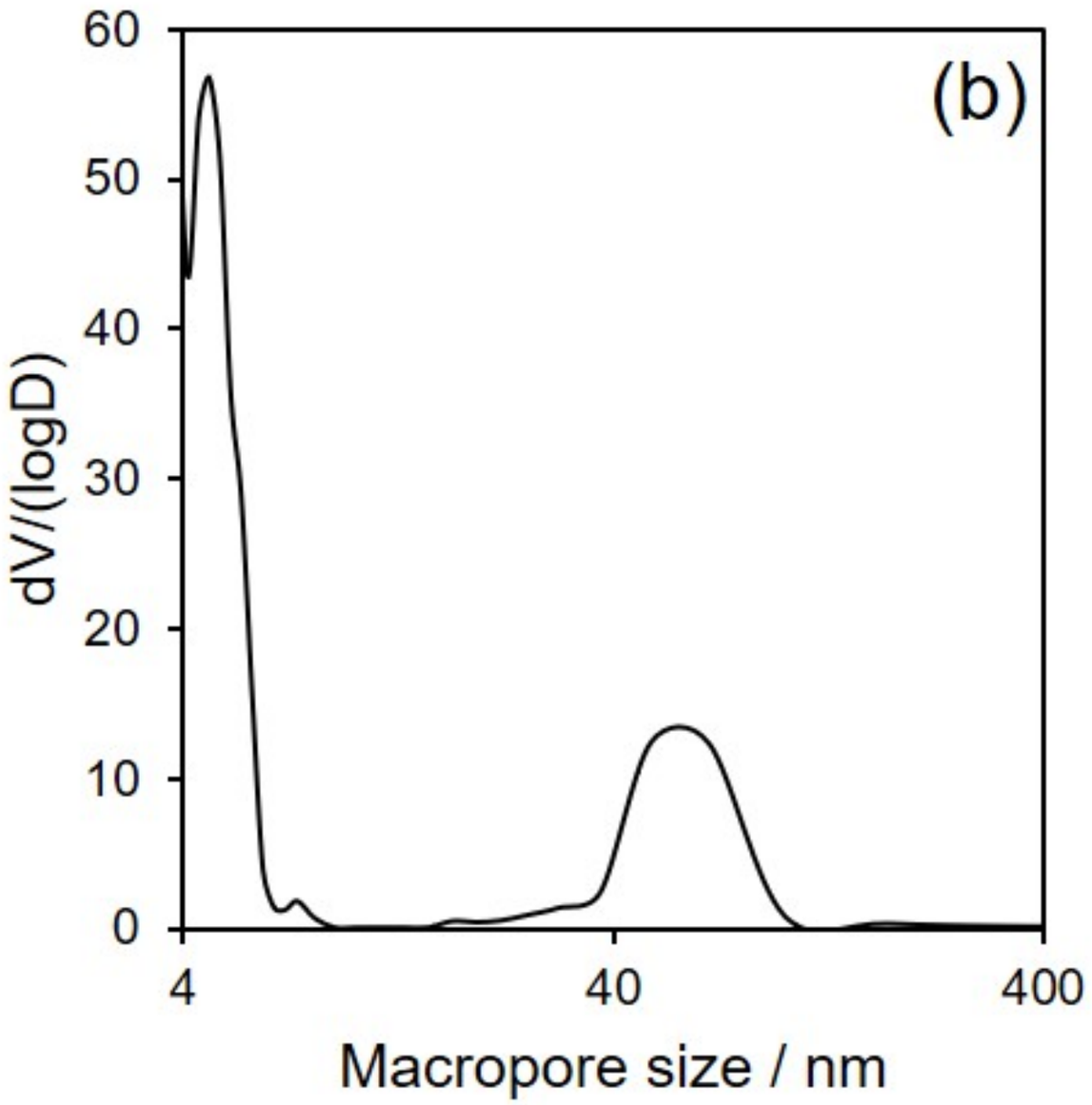
(b)
dV/(logD)
60
50
40
30
20
10
0
4
40
400
Macropore size / nm

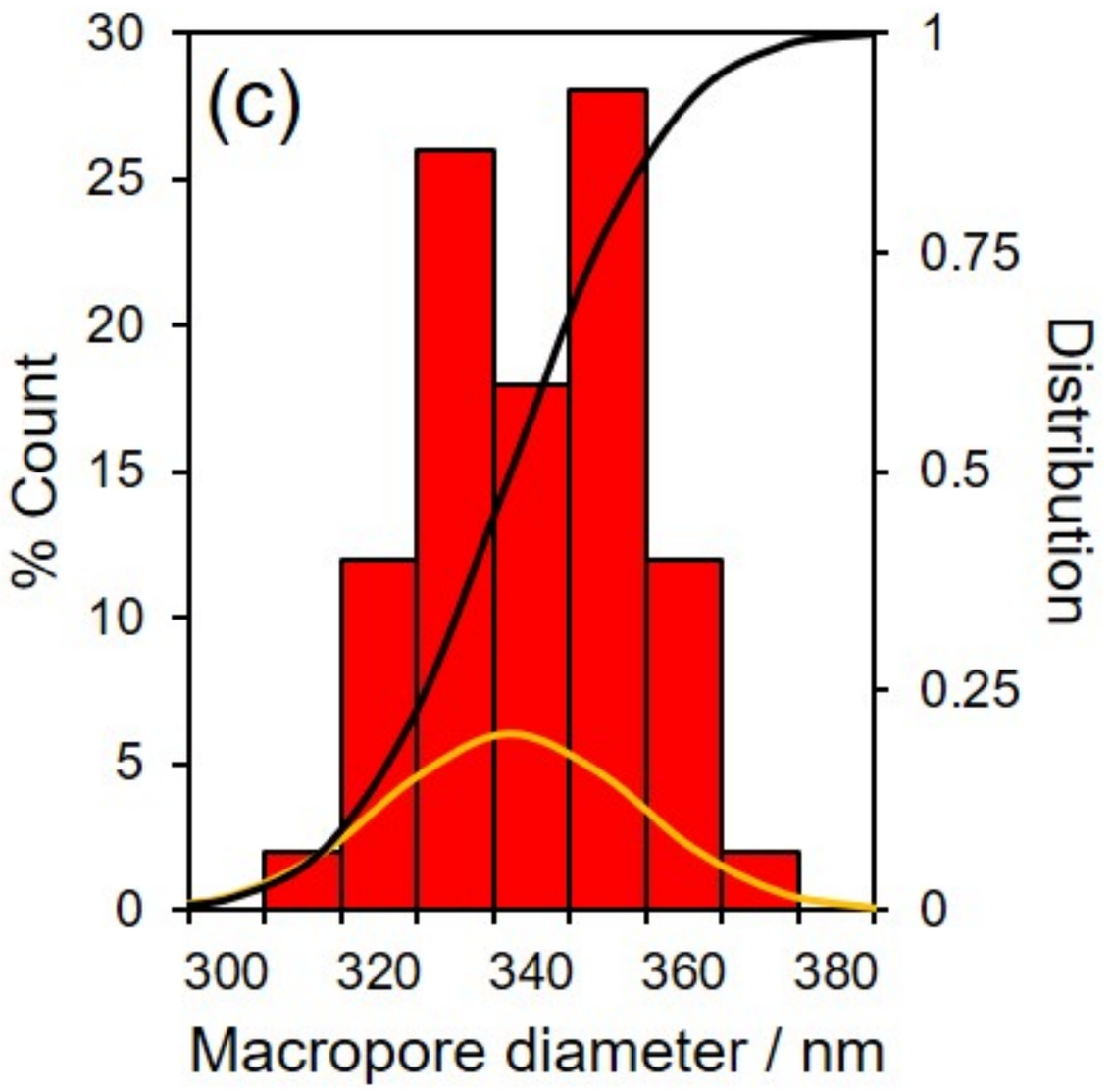
(c)
% Count
Distribution
30
25
20
15
10
5
0
1
0.75
0.5
0.25
0
300
320
340
360
380
Macropore diameter / nm

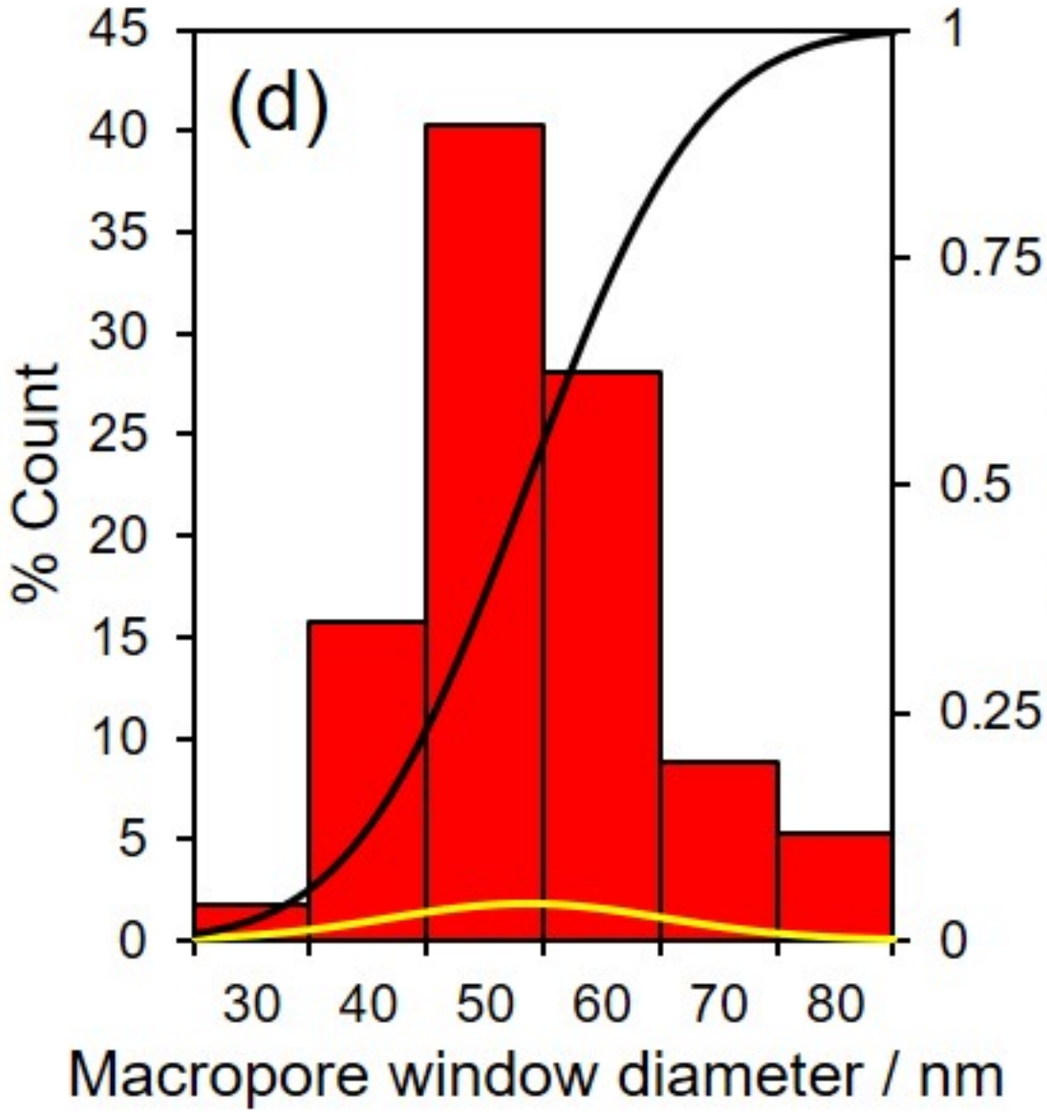
(d)
% Count
Distribution
45
40
35
30
25
20
15
10
5
0
1
0.75
0.5
0.25
0
30
40
50
60
70
80
Macropore window diameter / nm

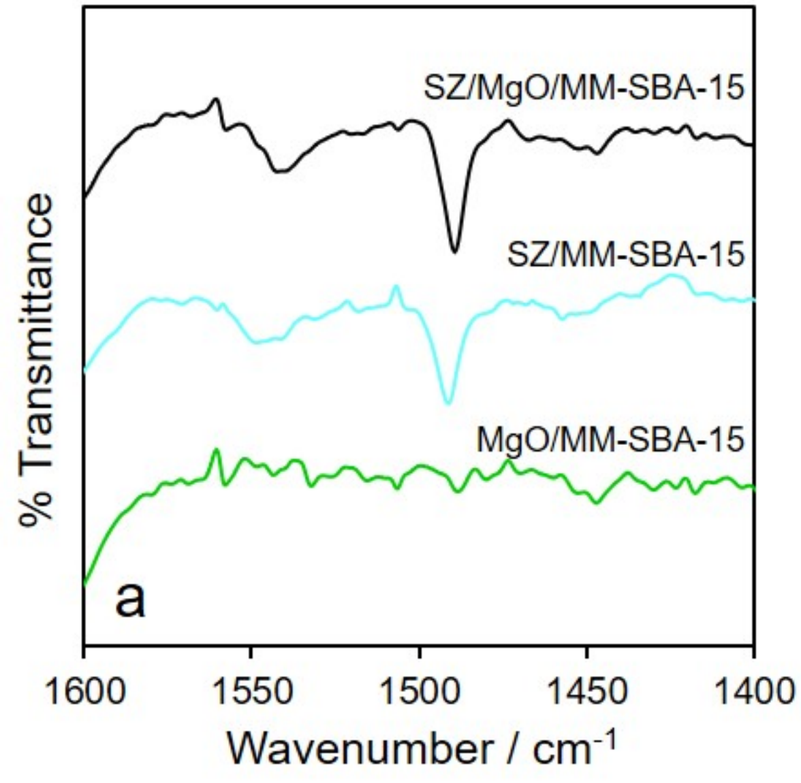
SZ/MgO/MM-SBA-15
SZ/MM-SBA-15
MgO/MM-SBA-15
% Transmittance
a
1600
1550
1500
1450
1400
Wavenumber / cm-1

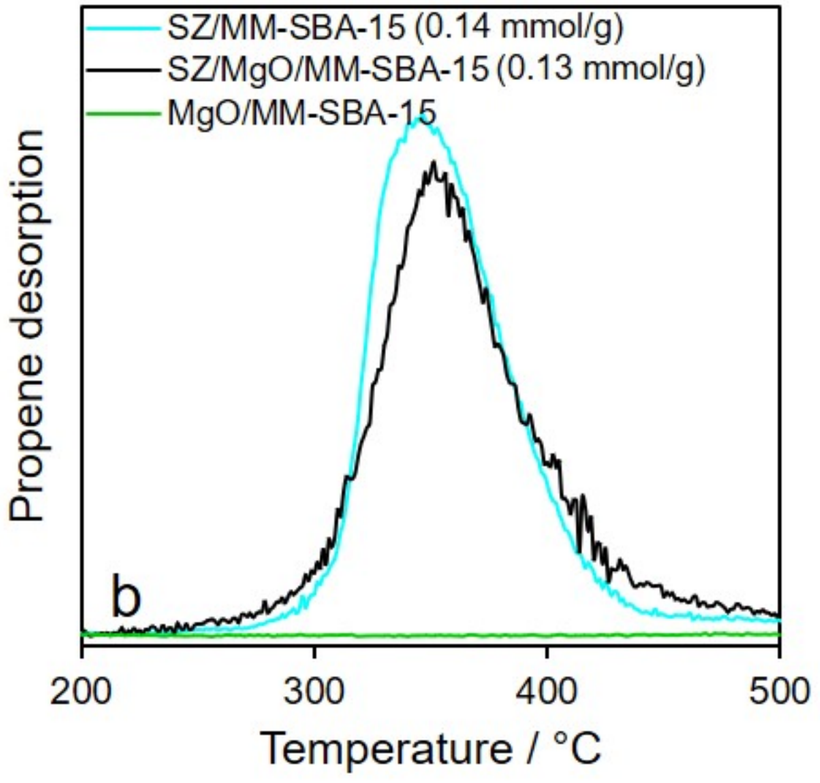
SZ/MM-SBA-15 (0.14 mmol/g)
SZ/MgO/MM-SBA-15 (0.13 mmol/g)
MgO/MM-SBA-15
Propene desorption
b
200
300
400
500
Temperature / °C

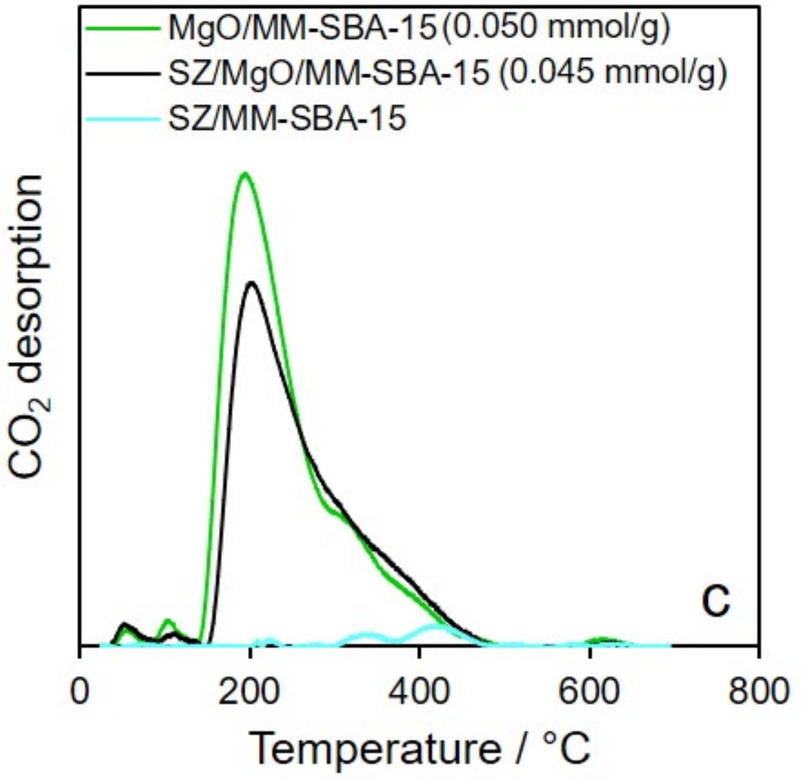
MgO/MM-SBA-15 (0.050 mmol/g)
SZ/MgO/MM-SBA-15 (0.045 mmol/g)
SZ/MM-SBA-15
CO2 desorption
c
0
200
400
600
800
Temperature / °C

Mesopores - COOH functionalised Pt NPs

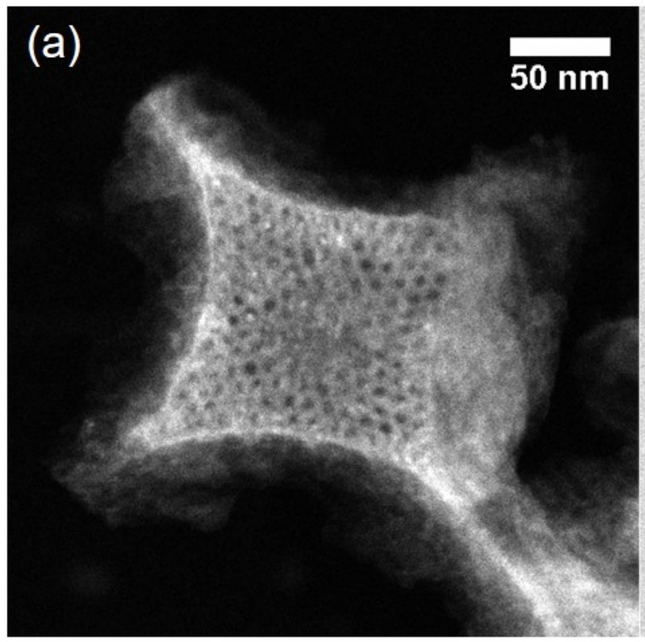

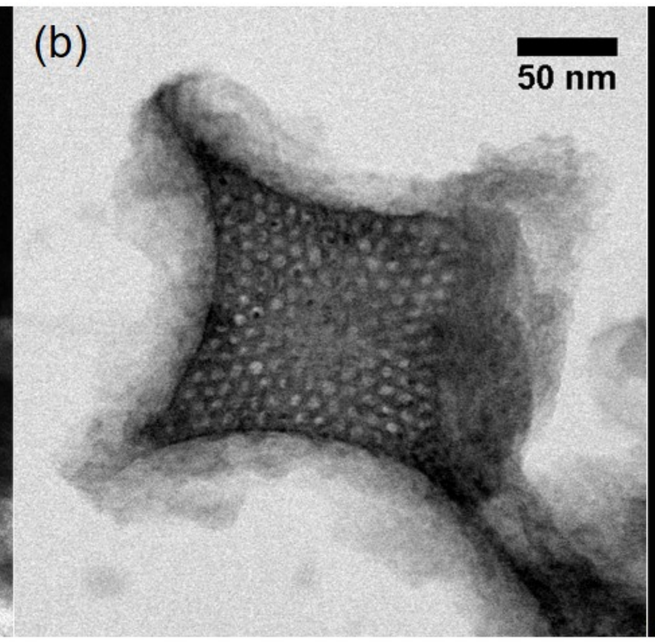

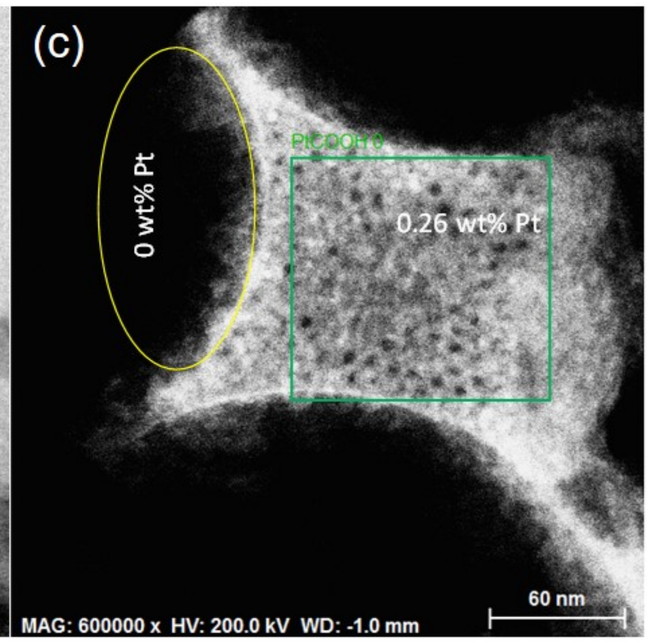

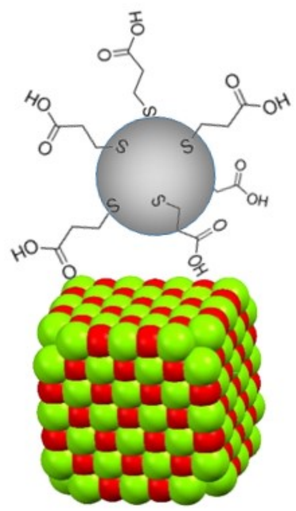

Macropores - NH_2 functionalised Pt NPs

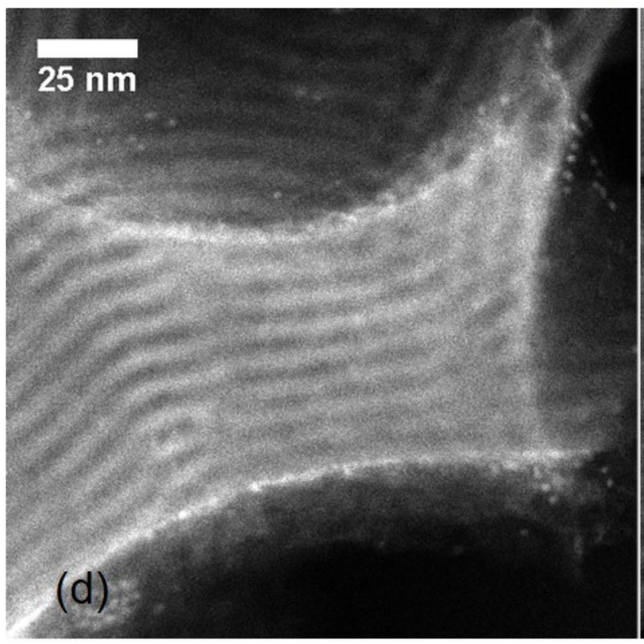

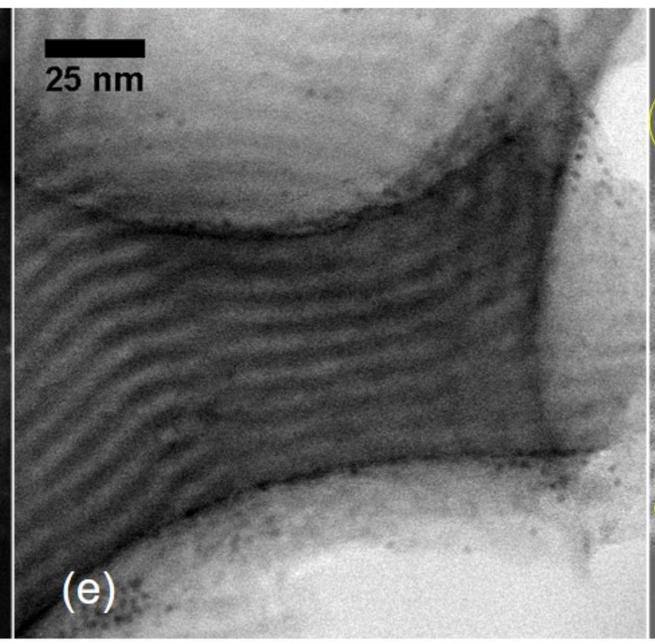

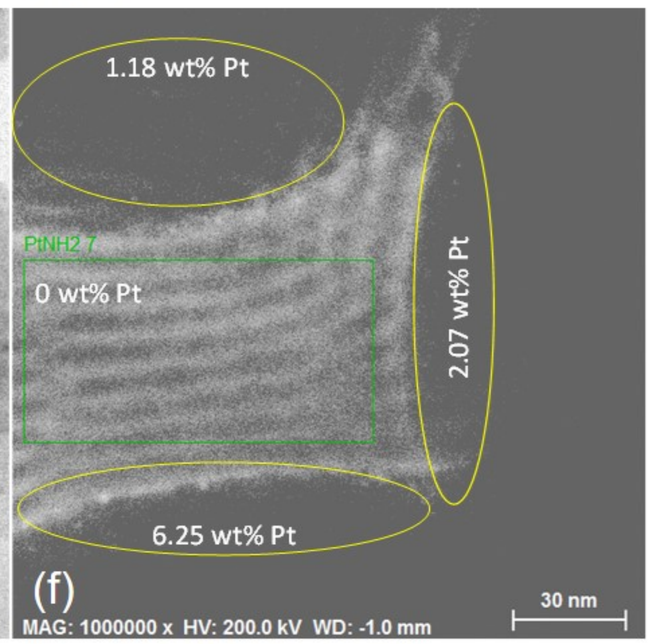

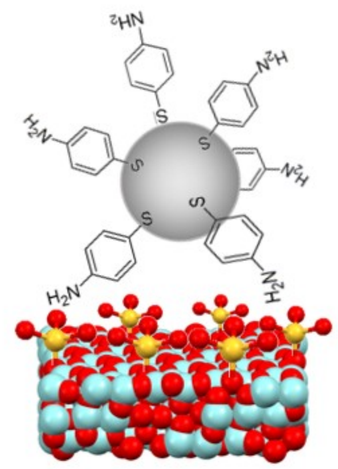

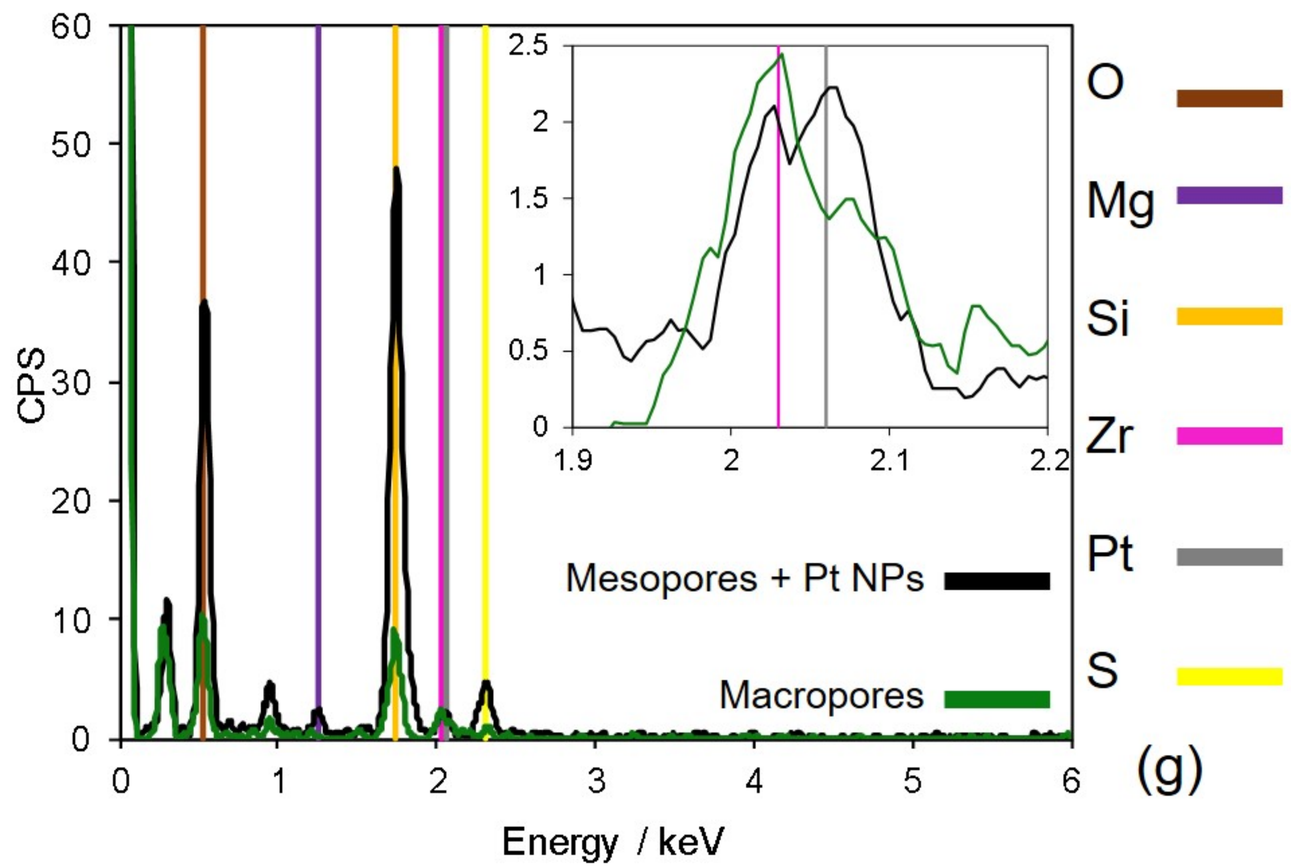

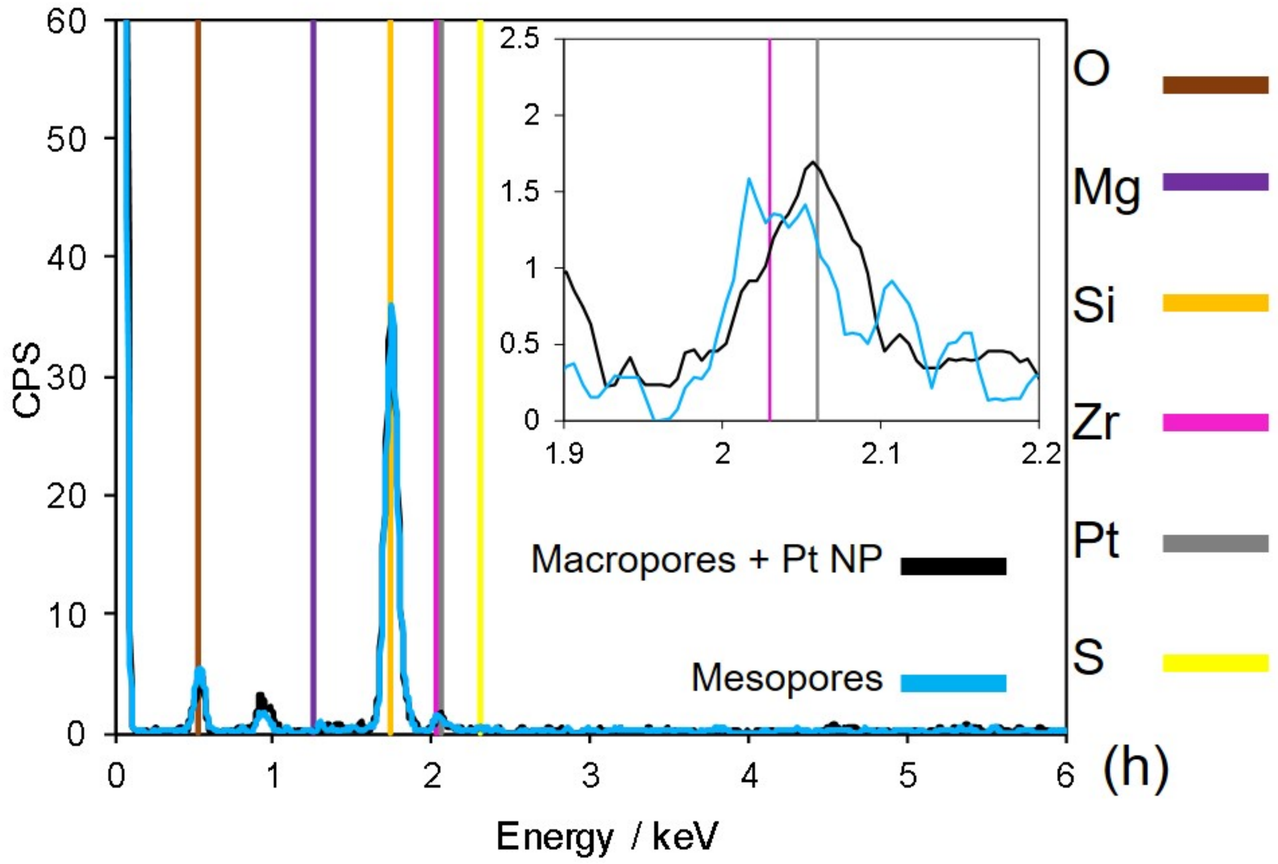

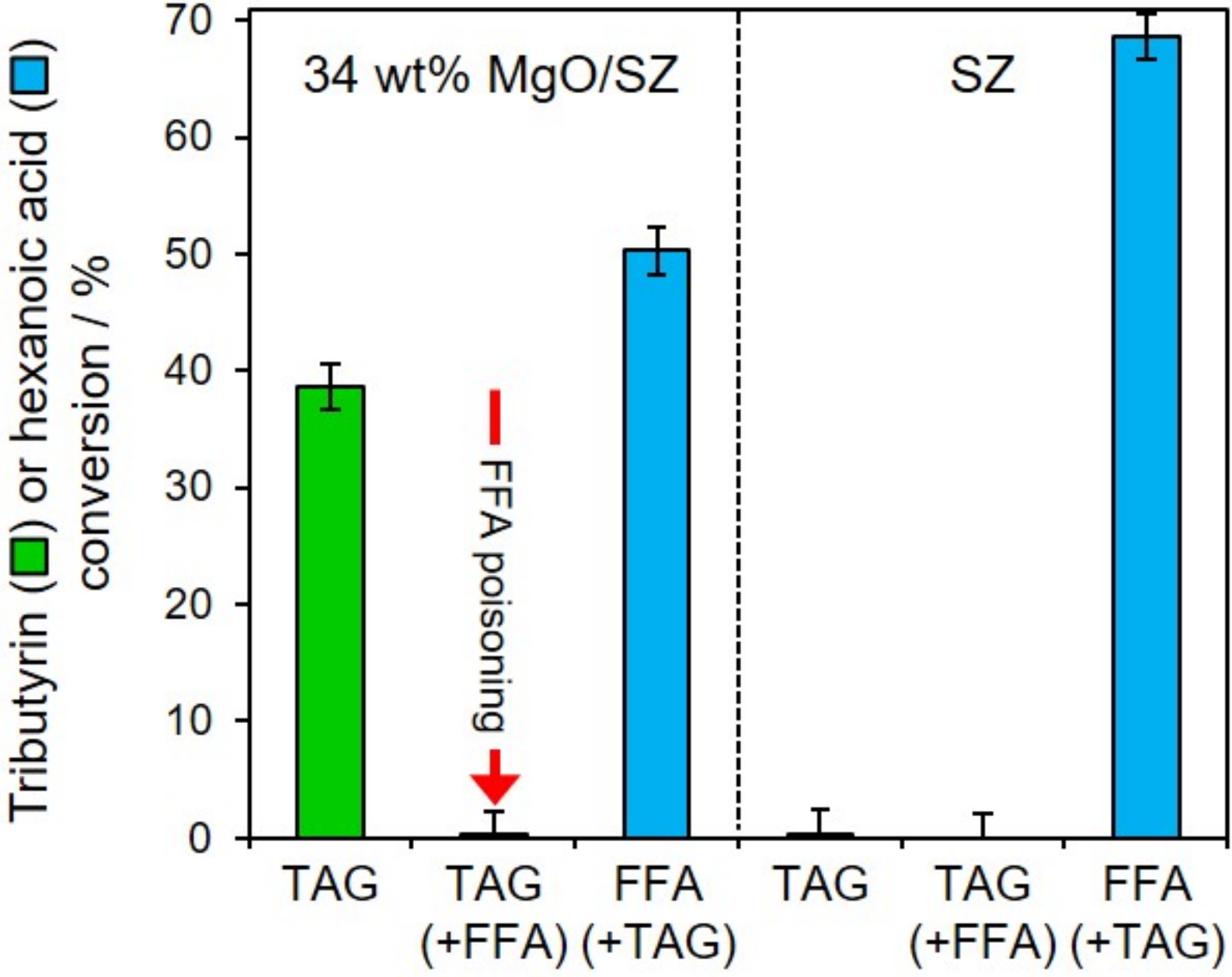
Tributyrin (■) or hexanoic acid (■)
conversion / %
70
60
50
40
30
20
10
0
34 wt% MgO/SZ
SZ
FFA poisoning
TAG
TAG (+FFA)
FFA (+TAG)
TAG
TAG (+FFA)
FFA (+TAG)

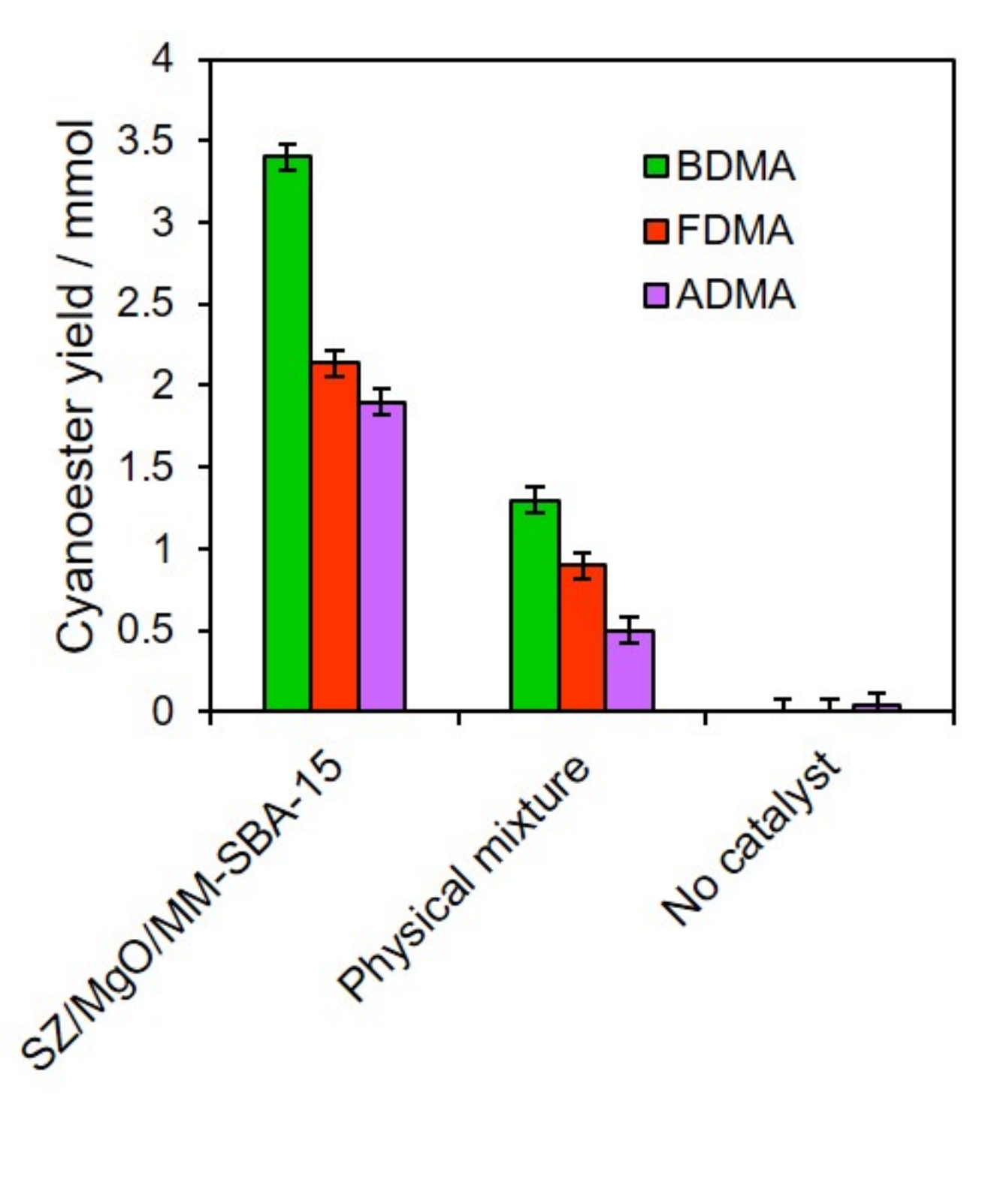
Cyanoester yield / mmol
4
3.5
3
2.5
2
1.5
1
0.5
0
BDMA
FDMA
ADMA
SZ/MgO/MM-SBA-15
Physical mixture
No catalyst

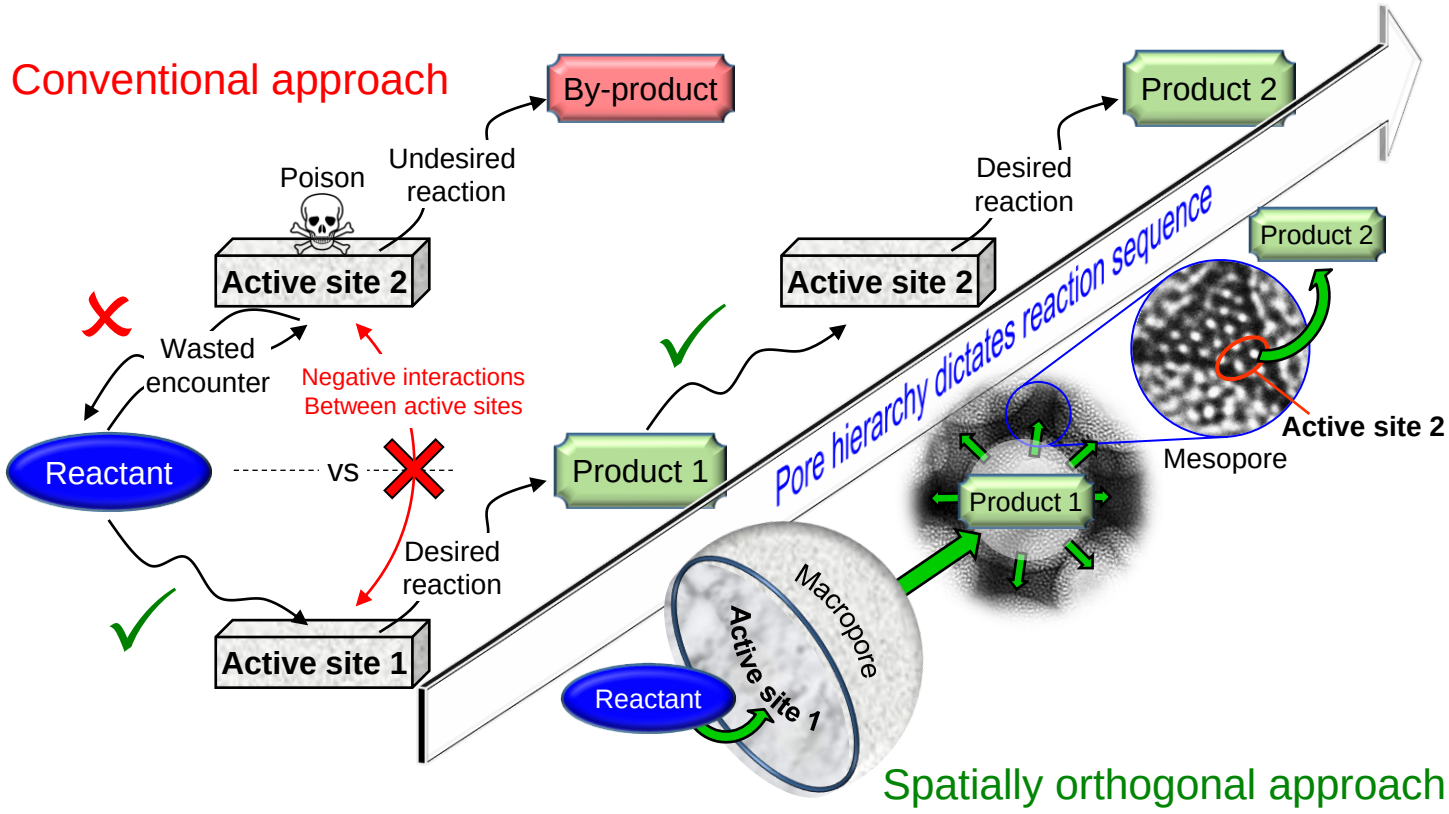
Conventional approach
By-product
Undesired reaction
Poison
Active site 2
Wasted encounter
Negative interactions Between active sites
Reactant
vs
Desired reaction
Active site 1
Product 1
Active site 2
Desired reaction
Product 2
Pore hierarchy dictates reaction sequence
Product 2
Active site 2
Mesopore
Product 1
Macropore
Active site 1
Reactant
Spatially orthogonal approach